Journal of Energy Storage 142 (2026) 119563

Contents lists available at ScienceDirect

Journal of Energy Storage

journal homepage: www.elsevier.com/locate/est

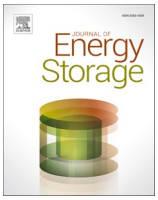

Research papers

Computational fluid dynamics analysis of energy and optical performance in fenestration systems incorporating solid-solid phase change materials

Hossein Arasteh [a,*], Wahid Maref [a], Hamed H. Saber [b]

[a] Department of Construction Engineering, École de Technologie Supérieure (ÉTS), University of Quebec, Montreal, QC, H3C 1K3, Canada
[b] Deanship of Research and Industrial Development, and Mechanical Engineering Department at Jubail Industrial College, Royal Commission of Jubail and Yanbu, Jubail Industrial City, 31961, Saudi Arabia

ARTICLE INFO

Keywords:
Building energy
Solid-solid phase change material
Glazing system
Zero energy buildings
Computational fluid dynamics

ABSTRACT

This study investigates the energy and optical performance of a double-glazed window system incorporating a solid-solid phase change material (DGW-SSPCM) compared to a conventional reference system (DGW-R). Transient CFD simulations were conducted using ANSYS FLUENT for the hottest and coldest days in Montreal, Canada, under sunny and cloudy conditions across four glazing orientations. A 2 mm SSPCM layer was applied to the interior pane, and natural convection (NC) within the glazing air gap was modeled using the solidification/melting and Discrete Ordinates models. Results show that NC has negligible effects during summer due to weak buoyancy-driven airflow, making its inclusion unnecessary for accurate energy and optical analysis under warm conditions. In winter, however, NC significantly impacts the phase change behavior and total energy performance of the system, with heat losses being underestimated by 10 to 23 % when NC is not considered. This behavior is supported by air gap velocity vector analyses, which show well-defined convective loops in winter with air velocities reaching up to 0.14 m/s, Reynolds numbers up to 57, and Rayleigh numbers exceeding 10^4, while summer flows remain weak and conduction-dominated. While the DGW-SSPCM system offers no substantial energy savings in summer due to nighttime thermal discharge, it achieves winter energy savings of up to 7.6 % and improves indoor thermal comfort. The optical analysis in this study has demonstrated that benefiting from the full cycle of the SSPCM phase transition allows the glazing to remain fully transparent during office hours, making it particularly practical for commercial buildings. The south-facing configuration, incorporating an SSPCM layer with a transition temperature of 15 °C on the interior pane, is identified as the optimal setup. This design ensures full transparency and thermal neutrality throughout the year during office hours, while maximizing latent heat utilization for effective thermal regulation in winter. These findings highlight the potential of SSPCM-integrated glazing systems as a passive strategy for enhancing energy efficiency and indoor comfort in heating-dominated climates, particularly in commercial buildings with daytime occupancy.

1. Introduction

Most individuals spend the majority of their time inside buildings. As living standards have improved, the role of buildings in global energy use has grown substantially, now accounting for nearly 40 % of total consumption and up to 35 % of greenhouse gas emissions, both of which contribute directly to climate change [1]. In response to this issue, global sustainability agendas advocate for immediate efforts to address climate impacts. Various technological and design-based solutions have emerged to improve indoor thermal conditions. These range from passive architectural strategies and enhanced cooling methods to energy-efficient air conditioning systems and renewable energy integration [2].

The building envelope, which functions as the interface between internal spaces and external weather conditions, is responsible for over half of the total energy consumption in buildings [3]. Ensuring thermal stability indoors requires careful envelope design. Traditionally, this was accomplished by incorporating heavy construction materials to boost the building thermal mass and inertia. However, the widespread adoption of lightweight construction systems has resulted in many buildings underperforming in terms of thermal efficiency [4]. Consequently, improving envelope performance has become a key focus of recent studies. The building envelope consists of opaque and transparent components, each playing a distinct role in thermal performance. Opaque elements include walls, roofs, and floors, while transparent parts comprise windows, curtain walls, and skylights. Among these,

* Corresponding author.
E-mail addresses: hossein.arasteh.1@ens.etsmtl.ca (H. Arasteh), Wahid.Maref@etsmtl.ca (W. Maref), saberh@rcjy.edu.sa (H.H. Saber).

https://doi.org/10.1016/j.est.2025.119563
Received 11 August 2025; Received in revised form 28 October 2025; Accepted 17 November 2025
Available online 25 November 2025

Nomenclature

A	Area (m^2)
c_p	Specific heat capacity (J/kgK)
d	Air gap depth (m)
d'	Optical thickness (m)
E	Energy (J)
g	Gravitational acceleration (m^2/s)
h	Heat transfer coefficient (W/m^2K)
h_s	Sensible enthalpy (J/kg)
H	Enthalpy (J/kg)
ΔH	Latent heat (J/kg)
I	Radiation intensity (W/m^2)
ℓ	Air gap height (m)
L	Latent heat of fusion (kJ/kg)
n	refractive index
p	Pressure (Pa)
P_{atm}	Atmospheric pressure (Pa)
q''	Total heat flux through air gap (W/m^2)
$\vec{r}$	Position vector (m)
R	Specific gas constant for dry air (J/kgK)
Ra	Rayleigh number, $Ra = \frac{g\beta' \Delta T d^3}{\upsilon\alpha}$
Ra_{avg}	Time-averaged Rayleigh number
Re	Reynolds number, $Re = \frac{\rho V_{avg} d}{\mu}$
Re_{avg}	Time-averaged Reynolds number
s	Sample thickness (path length) (m)
$\vec{s}$	Direction vector
$\vec{s}'$	Scattering direction vector
t	Time (s)
T	Temperature (°C)
ΔT	Air gap temperature difference (°C)
V	Velocity (m/s)
$\vec{V}$	Velocity vector (m/s)
V_{avg}	Volume-averaged velocity (m/s)
x	x-direction coordinate
y	y-direction coordinate
z	z-direction coordinate

Greek symbols

α	Thermal diffusivity (m^2/s)
β	Transparency fraction
β'	Thermal expansion coefficient (K^{-1})
λ	Thermal conductivity (W/mK)
μ	Dynamic viscosity (kg/ms)
ρ	Density (kg/m^3)
σ_a	Absorption coefficient (m^{-1})
σ_s	Scattering coefficient (m^{-1})
τ	Transmittance
υ	Kinematic viscosity (m^2/s)
∅	Phase function
Ω'	Solid angle (rad)

Subscripts

op	Opaque
PCM	Phase change material
ref	Reference
tr	Transparent

Acronyms

DGW	Double-glazing window
NC	Natural convection
PCM	Phase change material
SLPCM	solid-liquid phase change material
SSPCM	solid-solid phase change material

fenestration systems are particularly critical, as they are responsible for the majority of heat loss (up to 60 %) thereby significantly affecting the overall energy efficiency of buildings [5]. A promising passive solution to this challenge is the incorporation of PCMs into glazing systems. Our recent research [6], extensively reviewed the integration of PCMs into glazing systems, demonstrating their potential to enhance thermal performance while reducing visual transparency.

Moghaddam et al. [7] reviewed glazing solutions for nearly zero-energy buildings and proposed an approach for selecting optimal systems. They found that considering energy performance, thermal comfort, cost, and environmental impact together enable informed glazing choices, and future studies could include glare and visual comfort. Ceviz et al. [8] found that adding phase change material in horizontal double-glazing improves energy storage and thermal comfort, with a 30 % area ratio of PCM to double-glazed test elements providing the best balance between cooling duration and light transmittance. Lu et al. [9] evaluated double-layer and multilayer phase change material glazing and found that the optimal configurations depend on climate, improving thermal regulation and energy savings. Nsaif et al. [10] found that adding phase change material along with blinders in triple-glazed windows reduced interior temperatures and increased time lag, though PCM solidification leakage remains a challenge. Uribe et al. [11] developed and validated a heat transfer model for double-clear PCM glazing and integrated it into EnergyPlus [12]. They found that PCM glazing increases the thermal inertia, and reduces the cooling energy consumption by up to 9.1 % and the cooling peak loads by up to 10.5 %. Shaik et al. [13] tested double-pane glazing filled with organic phase change materials and found that the 30-degree liquid mixture best reduced heat gain, energy costs, and carbon emissions while allowing natural daylight, whereas the solid-state mixtures blocked daylight. Hu et al. [14] found that 10 mm PCM glazing reduced temperature fluctuations, delayed peak temperatures, and maintained adequate daylighting, while thicker layers (15 and 20 mm) lowered energy storage and daylight performance. Yuan et al. [15] showed that triple-glazed windows with PCM and silica aerogel improve thermal regulation and energy savings subjected to cold and tropical climates. The cold climates benefit from reduced heat loss, while tropical climates achieve up to 74.8 % energy savings. Future work should address durability, PCM stability, and extreme climate performance. Zhang et al. [16] showed that the optical properties of PCM glazing units are strongly affected by the thermal parameters and layer thickness of the PCMs. They indicated that the common assumption in previous studies that optical properties are independent of thermal parameters is not valid, and the design strategies for such glazing units should be revised accordingly. In another study by Zhang et al. [17], they showed that during phase change, the transmittance and reflectance of PCM glazing units vary linearly, with most changes occurring in the solid-liquid stage and notable changes in the solid-solid stage. Also, they have showed that an optimized radiative transfer model based on their findings reduced calculation errors compared to previous models. Mandev [18] found that integrating PCM in double-glazed windows improved the thermal regulation but reduced the natural light. A 45 % area ratio of PCM to window cut light transmittance by about one-third highlighting a trade-off between thermal comfort and visual transparency.

As provided above, the use of PCMs can regulate heat transfer through phase changes, either from solid to liquid, referred to as SLPCMs, or from solid to solid, referred to as SSPCMs. The present study adopts SSPCMs in glazing configurations due to their distinct advantages

over SLPCMs. These advantages include low subcooling effects, reduced material degradation, consistent optical behavior, the ability to be applied without encapsulation, absence of leakage, minimal phase segregation, small volumetric changes, and high thermal stability. Unlike SLPCMs, SSPCMs remain in a solid state throughout the phase transition and can be directly applied to the surface or pane of a multi-glazed window at a defined thickness. This configuration allows the low thermal conductivity of the intermediate air or inert gas layer to be preserved, maintaining the insulating function between indoor and outdoor environments. In contrast, SLPCMs, when used to fill the air gap, reduce the system thermal resistance due to their relatively higher thermal conductivity. Although encapsulation can address this drawback by stabilizing the SLPCM in a solid state, the performance still depends on containment and material compatibility. SSPCMs undergo a phase transition between a semi-crystalline (opaque) and an amorphous (transparent) state, wherein only the soft segments melt while the hard segments (polymeric backbones with significantly higher melting temperatures) retain structural stability. This transition allows the material to remain solid as the soft segments undergo phase change, anchored by the hard segments. Detailed descriptions of the SSPCM phase transition mechanism are available in [19].

Although numerous studies have examined the application of SLPCMs in glazing systems, research focusing on SSPCMs in smart glazing remains limited. Raj et al. [20] presented a review that outlined the development of SSPCMs and recent progress in their thermophysical properties. The study provided an extensive compilation of organic, polymeric, organometallic, and commercially available SSPCMs, including data on phase transition temperatures, melting points, molecular structures, and thermal behavior. This compilation serves as a valuable reference for professionals exploring SSPCM integration across a range of thermal energy applications. Another review [19] examined the relationship between molecular configurations, phase transition mechanisms, and thermal characteristics of SSPCMs. The study categorized SSPCMs into four primary groups: polymeric, organic, organometallic, and inorganic. It also offered guidelines for material selection based on specific thermal, mechanical, and physical requirements, supported by detailed listings within each category.

Guldentops et al. [21] evaluated the performance of SSPCMs in a passive building enclosure system installed on the south-facing facade of a structure in central Massachusetts. The analysis, conducted through a finite element model, considered both summer and winter scenarios to identify optimal seasonal configurations. The study emphasized the importance of refining extinction coefficients and phase transition temperatures to ensure year-round effectiveness. In a separate investigation, Gao et al. [22] conducted a numerical study involving a thin SSPCM layer integrated on the interior surface of a double-glazed window. Since EnergyPlus could not directly simulate latent thermal storage, an equivalent model was developed. Results indicated that a 3 mm SSPCM layer improved energy performance in warm, mixed, and cold climates, offering better results than conventional low-emissivity glazing. *Ma* et al. [23] investigated a composite glazing system combining silica aerogel with SSPCM for use in extremely cold regions of China. EnergyPlus was used for thermal analysis and Radiance for daylighting assessment. As with previous studies, an equivalent SSPCM model was required. Key influencing parameters identified through sensitivity analysis included transition temperature, latent heat, absorption coefficient, and refractive index. The study recommended a 10 mm aerogel layer to achieve energy savings while meeting daylighting requirements. Wang et al. [24] developed an inverse modeling approach to determine temperature-dependent equations for extinction coefficients and refractive indices of SSPCMs in the translucent phase. Constant values were used for the opaque and transparent phases, and the optical parameters derived were used in the current analysis. More recently, Zhang et al. [26] investigated SSPCM glazing windows as an alternative to SLPCM to avoid liquid leakage issues. Through a parametric study in cold weather, they found that the melting temperature and latent heat of the PCM strongly affect thermal performance, energy saving potential, and inner surface temperature, while optical properties such as absorption coefficient and refractive index have smaller effects. Optimal values yielded the highest energy saving efficiency of 15.38 %. Also, their study highlights guidelines for SSPCM design, noting that longer-term evaluations are needed for practical applications.

The reviewed literature highlights a clear gap in the application of SSPCMs in glazing systems, particularly in relation to energy performance assessment as well as optical evaluation through three-dimensional modeling. While SSPCMs offer latent heat storage benefits without the drawbacks of liquid-phase formation and moisture-related risks within the building envelope, existing numerical studies are limited. Most prior investigations have either employed EnergyPlus, which lacks the capability to accurately capture phase transition phenomena and thus requires equivalent modeling approaches, or utilized two-dimensional models that assume the SSPCM fully occupies the air gap in the glazed units. To address these limitations, a three-dimensional CFD model using the finite volume method is developed in this study to evaluate the energy and optical performance of a double-glazed window system incorporating SSPCMs. The model accounts for all modes of heat transfer in the double-glazed system, including natural convection (NC) that has resulted due to buoyancy-driven flow within the air gap. In this study, the SSPCM layer is positioned onto the interior surface of the air gap-facing glass pane, enabling the material to maintain elevated temperatures and remain in its transparent state throughout the year. This study aims to provide a more comprehensive understanding of DGW-SSPCM behavior under various climatic and operational scenarios via 3D CFD modeling. Following model validation, a parametric study was conducted to compare the performance of the DGW-SSPCM system with and without accounting for NC effects. The analysis was carried out under both sunny and cloudy conditions for the cold-dominant climate of Montreal. Simulations were performed for the four principal window orientations (north, east, south, and west) on the coldest and hottest days of the year 2022. This investigation also aims to evaluate the influence of NC on the heat transfer and fluid flow characteristics of the system across different façade orientations.

2. Methodology

2.1. Model geometry

This study investigates two window configurations across four orientations: North, East, South, and West. The first configuration is a conventional DGW with an air gap, designated as DGW-R. The second, referred to as DGW-SSPCM, incorporates a 2 mm layer of SSPCM applied to the inner surface of the interior glass pane. Both glazing systems consist of two glass panes, each measuring 200 mm by 200 mm with a thickness of 4 mm. In the DGW-R setup, the panes are separated by a 16 mm air gap, as shown in Fig. 1a. For the DGW-SSPCM configuration, the air gap is reduced to 14 mm to accommodate the SSPCM layer while preserving the total thickness of the window unit, as shown in Fig. 1b.

2.2. Material properties

The glazing system examined in this study consists of two clear glass panes, each 4 mm thick and possessing an emissivity of 0.9 [27]. The corresponding thermophysical and optical properties of the glass were sourced from [28], while the selected SSPCM was adopted based on the material specifications provided in [29]. Optical characteristics of the SSPCM, including refractive index along with absorption and scattering coefficients, were determined using the correlations proposed in [24]. Table 1 summarizes the thermophysical properties of all materials utilized in the simulations. In this study, one SSPCM material was used with identical thermophysical properties for both transition temperatures, set to 15 °C for winter and 25 °C for summer.

For the SSPCM used in this study, the refractive index and extinction

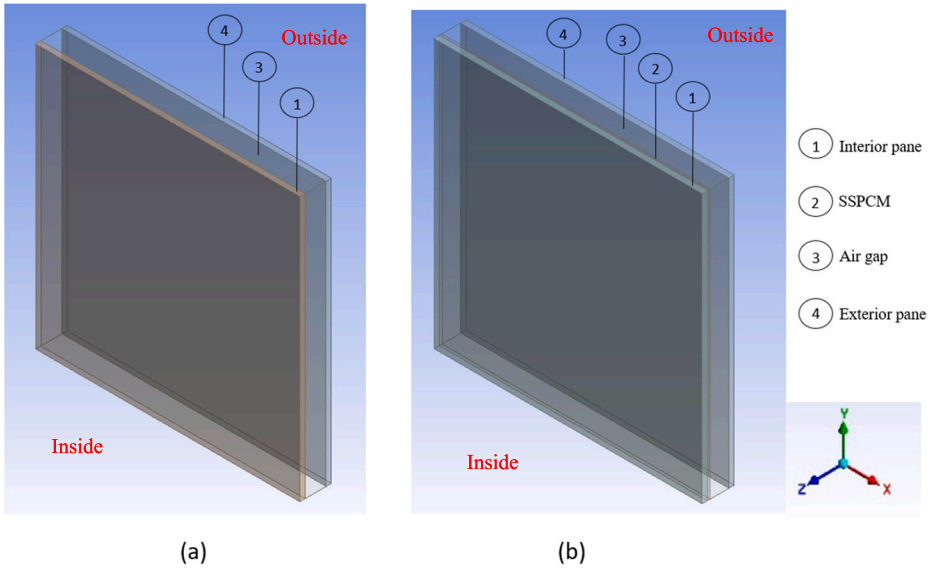

Fig. 1. Current study model geometry: (a) DGW-R and (b) DGW-SSPCM.

Table 1
Thermophysical and optical properties of materials.

Material	Density (kg/m3)	Specific heat (J/kgK)	Thermal conductivity (W/mK)	Absorption coefficient (1/m)	Scattering coefficient (1/m)	Refractive index
Air	f (P, T)	1006.43	0.0242	0	0	1
Glass	2500	840	1.3	19	0	1.5
SSPCM	1055	1630	0.36	33.80 (β = 1) 25.73 (β = 0)	0 (β = 1) 119.02 (β = 0)	1.11 (β = 1) 5.33 (β = 0)

coefficient are specified as 1.11 m^{-1} and 25.73 m^{-1} for the transparent phase, and 5.33 m^{-1} and 152.82 m^{-1} for the opaque phase, respectively, based on values reported in [30]. To evaluate the optical behavior of the SSPCM in its intermediate (translucent) state, Eqs. (1) and (2) are employed. These equations compute the average optical properties as functions of the transparency fraction, a term adopted in place of the conventional "liquid fraction" since SSPCMs do not undergo a liquid phase. The transparency fraction, β, quantifies the proportion of the material in the transparent state, where $\beta = 0$ corresponds to a fully opaque material and $\beta = 1$ indicates full transparency. A transparency fraction of zero implies that the SSPCM temperature is at or below the lower boundary of the transition temperature range, referred to as the *opaqueus* temperature (analogous to the *solidus* temperature in solid-liquid phase change materials, SLPCMs), indicating a fully opaque phase. In contrast, a value of one signifies that the temperature has reached or exceeded the upper boundary, referred to as the *transparentus* temperature (analogous to the *liquidus* temperature in SLPCMs), resulting in a fully transparent phase. Intermediate values of β between 0 and 1 reflect a translucent state, comparable to the mushy zone observed in SLPCMs.

$$\sigma_{a,\ cell} = 33.8\beta + 25.73(1-\beta) \tag{1}$$

$$\sigma_{s,\ cell} = 119.02(1-\beta) \tag{2}$$

It should be noted that the transparency level of 1.0 corresponds to the SSPCM being in its fully transparent phase, which is similar to the fully liquid phase of a SLPCM. This does not mean that the material is permanently or fully transparent, but rather that it has reached the phase where light can pass through with minimal scattering. Therefore, reporting a transparency of 1.0 in this study indicates that the material is at its maximum transparent state during the phase transition.

2.3. Governing equations

The modeling of SSPCM is based on the enthalpy-porosity method within the ANSYS Fluent software [31]. A very high viscosity is assigned to the SSPCM to suppress internal flow, ensuring a nearly static state. Simulations are conducted for both cases, with and without NC in the air gap of the DGW for both configurations: DGW-SSPCM and DGW-R. This approach allows for accounting for the effect of NC in the air gap to accurately assess the energy performance of both DGW-SSPCM and DGW-R systems. The analysis uses the climate of Montreal as a representative cold-dominant city to assess the potential energy savings relative to conventional glazing systems.

The governing equations, including the Discrete Ordinates (DO) model for radiation and the solidification/melting model for representing SSPCM phase transitions, are:

- Mass conservation equation [31]:

$$\frac{\partial \rho}{\partial t} + \nabla.(\rho \vec{v}) = 0 \tag{3}$$

- Momentum conservation equation [31]:

$$\frac{\partial}{\partial t}(\rho \vec{v}) + \nabla.(\rho \vec{v}\,\vec{v}) = -\nabla p + \nabla.(\mu \nabla \vec{v}) + \rho \vec{g} + S_m \vec{v} \tag{4}$$

In Eqs. (3) and (4), ρ, t, $\vec{v}$, p, and μ represent density, time, velocity vector, pressure, and dynamic viscosity, respectively. It is important to note that the source term "$S_m \vec{v}$" is included on the right-hand side of Eq. (7) as part of the solidification/melting (i.e., SSPCM in this study) model. The term S_m is defined as the negative of the porosity function ($A_m(\beta)$), as described by Brent et al. [32]. This porosity function is formulated to ensure that the momentum equations resemble the

Carman-Kozeny equations [33], which are commonly used to describe fluid flow in porous media.

- Energy equation [31]:

$$\frac{\partial}{\partial t}(\rho H) + \nabla.(\rho \vec{v} H) = \nabla.(k\nabla \mathrm{T}) + \mathrm{S}_h \tag{5}$$

In Eq. (8), the enthalpy of the PCM, H, is calculated as the sum of the sensible enthalpy, h_s, and latent heat, ΔH as:

$$H = h_s + \Delta H, \tag{6}$$

where,

$$h_s = h_{s,ref} + \int_{T_{ref}}^{T} c_p dT \tag{7}$$

In Eq. (8), the fractional latent heat of the PCM, ΔH, is defined based on the material's latent heat of fusion, L. As provided in Eqs. (9) and (10), the value of ΔH ranges from 0 in the opaque phase ($\beta = 0$), to L in the transparent phase ($\beta = 1$), and takes intermediate values between 0 and L when the temperature lies within the transition range, $T_{opaqueus} < T < T_{transparentus}$, corresponding to the translucent phase.

$$\Delta H = \beta L \tag{8}$$

In this study, the transparency fraction is calculated as follows:

$$\beta = \begin{cases} 0 & if\ T \le T_{opaqueus} \\ 1 & if\ T \ge T_{transparentus} \\ \dfrac{T - T_{opaqueus}}{T_{transparentus} - T_{opaqueus}} & if\ T_{opaqueus} < T < T_{transparentus} \end{cases} \tag{9}$$

The term S_h in Eq. (5) represents the volumetric heat source or sink associated with the phase change and is defined as:

$$S_h = -\frac{\partial(\rho \Delta H)}{\partial t} \tag{10}$$

- Radiation equation:

In this study, the Discrete Ordinates (DO) model is employed to simulate radiative heat transfer due to its comprehensive capability in radiation modeling within ANSYS Fluent [31]. The model facilitates accurate representation of radiation scattering and absorption across a wide range of optical thicknesses. It operates by transforming the radiative transfer equation into a set of transport equations for radiation intensity, which are solved over a finite number of discrete solid angles [31]. While the DO model improves accuracy, it also increases computational demand by requiring the solution of additional equations, thereby extending the simulation time.

For a position vector, the radiative transfer equation for a medium that absorbs, emits, and scatters radiation at position $\vec{r}$ in the direction $\vec{s}$ is given as follows [31]:

$$\frac{dI(\vec{r}, \vec{s})}{ds} + (\sigma_a + \sigma_s) I(\vec{r}, \vec{s}) = an^2 \frac{\sigma T^4}{\pi} + \frac{\sigma_s}{4\pi} \int_0^{4\pi} I(\vec{r}, \vec{s}') \varnothing(\vec{s}.\vec{s}') d\Omega' \tag{11}$$

The DO model treats the radiative transfer equation in the direction $\vec{s}$ as a field equation, expressed as follows [31]:

$$\nabla.(I(\vec{r}, \vec{s})\vec{s}) + (\sigma_a + \sigma_s) I(\vec{r}, \vec{s}) = an^2 \frac{\sigma T^4}{\pi} + \frac{\sigma_s}{4\pi} \int_0^{4\pi} I(\vec{r}, \vec{s}') \varnothing(\vec{s}.\vec{s}') d\Omega' \tag{12}$$

In Eqs. (11) and (12), I, n, $\vec{r}$, $\vec{s}$, $\vec{s}'$. $\varnothing$, Ω', and σ indicate radiation intensity, refractive index, position vector, direction vector, scattering direction vector, phase function, solid angle, and the Stefan-Boltzmann constant (5.67×10^{-8} W/m^{2}K^4), respectively.

The energy performance of the different glazing systems in this study are evaluated using the Eq. (13). The area-averaged heat flux in this equation has been calculated in the interior surface of the glazing system.

$$E = q''_{avg} \times t \times A \tag{13}$$

$$\langle q'' \rangle_A = q''_{avg} = \frac{1}{A} \int_A q''(x, y) dA \tag{14}$$

2.4. Initial and boundary conditions

The glazing system analyzed in this study is evaluated across four orientations (North, East, South, West) in Montreal, Quebec, Canada, located at 45.52°N latitude and 73.42°W longitude. The selected dates representing the coldest and hottest days of the year are found to be in January 22 and July 21, 2022, respectively. Montreal follows GMT-5 during Eastern Standard Time (EST) and GMT-4 during Eastern Daylight Time (EDT). According to the Köppen–Geiger climate classification [34], Montreal falls under the Dfb category, indicating a humid continental climate characterized by warm summers and no distinct dry season. Simulations are conducted under both sunny and cloudy conditions for the identified extreme days. The climatic inputs used in the analysis include hourly wind speed [35], ambient temperature [35], direct solar irradiation [31], and diffuse solar irradiation [31].

The initial temperature is set to 18 °C for all the studied cases. In our previous study [36], the DGW-SSPCM system reaches a stabilized energy and optical state after two simulation days, showing the influence of the initial conditions on the system performance is negligible beyond this point. Accordingly, in this study, all simulations are carried out over a 48-h period, with the first 24 h serving as a preconditioning phase to eliminate the influence of initial conditions, and the subsequent 24 h used for performance analysis.

The side surfaces of the window system, including the exterior top, bottom, front, and back, are treated as thermally insulated or adiabatic, indicating that no heat transfer occurs through these boundaries. The interfaces between adjacent material layers are modeled using coupled thermal boundary conditions and semi-transparent radiation boundary conditions. These conditions ensure continuity of temperature and heat flux across both real and shadow surfaces, while also allowing incoming radiation to be transmitted through the interface. All material layers are assumed to be in perfect thermal contact, which means that thermal contact resistance at each interface is set to zero.

Mixed thermal boundary conditions, consisting of both convection and radiation, are applied to the indoor and outdoor surfaces of the window. Therefore, it is necessary to define parameters such as the heat transfer coefficient, free stream temperature, surface emissivity, and radiation temperature for these surfaces. In order to account for solar radiation in the numerical model, semi-transparent radiation boundary conditions are used. This requires defining direct and diffuse solar irradiance, along with beam direction vectors in the x, y, and z directions for both indoor and outdoor boundaries. The emissivity of standard clear glass is set to 0.9 [27] across all boundaries. A sunshine factor of 1 is used to represent sunny conditions, while a value of 0 is used for cloudy conditions, resulting in zero direct solar irradiation under overcast skies.

For the thermal and radiation boundary conditions on the indoor surface of the window, the heat transfer coefficient is specified as 8.7 W/m^2·K [37]. The free stream temperature and external radiation temperature on the indoor surface of the window are set to 26 °C for summer and 22 °C for winter [37]. No solar radiation is applied to the indoor surface to avoid modeling direct or diffuse solar gains from indoor sources.

For the outdoor surface boundary conditions, all parameters except emissivity are implemented into ANSYS Fluent using User Defined

Functions (UDFs) written in the C programming language, in accordance with the Fluent framework, to simulate a complete 24-h period. These UDFs apply piecewise linear functions to input hourly weather data. Hourly ambient temperature values are used for the free stream temperature, and the radiation boundary conditions are defined using hourly values of direct and diffuse solar irradiation, along with corresponding beam direction vectors. The hourly heat transfer coefficient, determined based on wind speed, and the external radiation or sky temperature, calculated from ambient temperature, are evaluated using Eqs. (15) and (16) [38].

$$h_a = 5.62 + 3.9\, v_{wind} \tag{15}$$

$$T_{sky} = 0.0552\, T_{air,o}^{1.5} \tag{16}$$

In Eq. (15), h_a is expressed in W/m^{2}K and v_{wind} in m/s. In Eq. (16), both T_{sky} and $T_{air,o}$ are given in Kelvin.

3. Numerical model

3.1. Modeling approach

The commercial CFD software ANSYS Fluent (version 2022 R1) is employed to perform three-dimensional simulations using the finite volume method. The computational geometry is generated in Design Modeler, and meshing is carried out using Ansys Meshing. The SIMPLE (Semi-Implicit Method for Pressure-Linked Equations) algorithm is used for velocity-pressure coupling. A second-order upwind scheme is applied for the discretization of pressure, momentum, and energy equations, while the Discrete Ordinates (DO) radiation model and transient formulation are discretized using a first-order upwind scheme and a first-order implicit scheme, respectively. The convergence criteria are set to 10^{-6} for mass conservation, x-velocity, y-velocity, and z-velocity, and to 10^{-9} for both the energy equation and DO radiation intensity.

To prevent direct interaction between the SSPCM and the adjacent air gap, a 0.001 mm thick transparent glass layer is inserted at their interface, addressing the software inability to simulate direct contact between distinct media. This artificial layer is defined with zero absorption and scattering coefficients, a refractive index of 1, and high thermal conductivity, ensuring that it has no impact on the system energy or optical behavior. NC within the air gap is modeled by incorporating a gravitational body force, $\rho\vec{g}$ (with $g_x = 0.0$ m/s^2, $g_y = -9.81$ m/s^2, and $g_z = 0.0$ m/s^2), applied only to the air gap. This allows buoyancy-driven flow to be captured without influencing other materials in the domain. It should be noted that the momentum equation need not be solved in the SSPCM to reduce computational time, and the SSPCM can be treated as a solid domain. Accordingly, the model was re-run with the volume force applied only to the air gap. This approach significantly reduced computational time while yielding results identical to those obtained when the momentum equation was solved throughout the entire domain.

A constant transition range of 1 °C is used for the phase change process, with transition temperatures of 15 °C for winter and 25 °C for summer. These values are selected based on previous studies [39], which showed that they enable complete phase transition of the SSPCM. This setup allows full utilization of the material's latent heat storage capacity and facilitates the evaluation of system performance under both heating and cooling conditions.

In this research, the solidification/melting model traditionally applied to solid-liquid phase change materials (SLPCMs) is adapted for use with solid-solid phase change materials (SSPCMs). The primary distinction lies in the absence of a liquid phase in SSPCMs during the phase change process, which eliminates NC effects. By neglecting gravity and assigning a high viscosity to the liquid phase of the SLPCM, its behavior can be approximated to that of an SSPCM.

Assumptions considered in the numerical model are as follows:

1. The SSPCM layer is treated as a solid domain with no internal flow; the momentum equation is not solved within this layer.
2. The thermophysical properties of the SSPCM were considered identical for both cases with transition temperatures of 15 °C (winter) and 25 °C (summer) to isolate the effect of the transition temperature on the optical and energy performance of the glazing system.
3. Gravity is applied only to the air gap by specifying a source term (ρg) in the y-momentum equation ($g_x = 0$, $g_y = -9.807$ m/s^2, and $g_z = 0$) to capture the NC effects and buoyancy-driven flow.
4. Air in the gap is treated as a compressible gas to account for the natural convection inside the air layer.
5. Thermophysical properties of air and SSPCM are assumed constant, except for the density variation of air, which drives buoyancy effects.
6. Radiative heat transfer is modeled using the Discrete Ordinates (DO) method.
7. Heat conduction in glass and SSPCM is solved in three dimensions, with phase change in the SSPCM captured using the solidification/melting model.
8. The SSPCM transition temperature is fixed, and hysteresis effects are neglected.
9. Initial condition effects were eliminated by discarding the first 24 h of the simulation; all reported results correspond to the second 24-h period of the 48-h run to ensure that initial condition influences were eliminated from the numerical results.
10. Moisture transfer and condensation within the air gap are not accounted for in this study.
11. All interfaces between all layers of SSPCM, air gap and glass are assumed to be in perfect thermal contact (i.e., no interfacial thermal resistances at these interfaces)

3.2. Numerical model validation

To validate the numerical model incorporating the Discrete Ordinates (DO) radiation model and the solidification/melting model in glazing systems, transient numerical results over a 12,000-s simulation period are compared with experimental data reported by Gowreesunker et al. [28]. Their study investigated transmittance variations in PCM-filled glazing units over time. A specialized experimental setup was developed to monitor radiation effects during the mushy phase, which cannot be captured using a spectrophotometer alone. The setup was housed in an environmental chamber with controlled air temperature, and a 150 W metal halide lamp emitting diffuse neutral white light was used as the radiation source. The test specimen was a regular double-glazed unit measuring 20 cm by 20 cm, with an overall thickness of 24 mm. It consisted of two 4 mm glass panes separated by a 16 mm air gap. In the PCM-filled configuration, the air gap was replaced with RT27. The initial air gap temperature and irradiation level were set at 13 °C and 950 W/m^2, respectively.

The experimental transmittance data from Gowreesunker et al. [28] is used to validate the numerical model. This data is illustrated in Fig. 2a by the black dashed curve, with corresponding uncertainty bounds indicated by gray dashed curves. In Fig. 2, transmittance is defined as the ratio of radiation flux transmitted through the front and back surfaces. The post-processing procedure for transmittance calculation in the present study follows the same equations and methodology described in the study of Gowreesunker et al. [28] and is represented in Eqs. (17) to (19). The simulation results, represented by the red curve, show strong agreement with the experimental measurements, remaining within the defined margin of error. The transmittance trends observed in both datasets also exhibit consistent behavior over time. Some discrepancies between the numerical and experimental results are noticeable in certain regions of the curve. These are attributed to the enthalpy-porosity model, which assumes a linear relationship between temperature and liquid fraction within the phase change range. This model treats

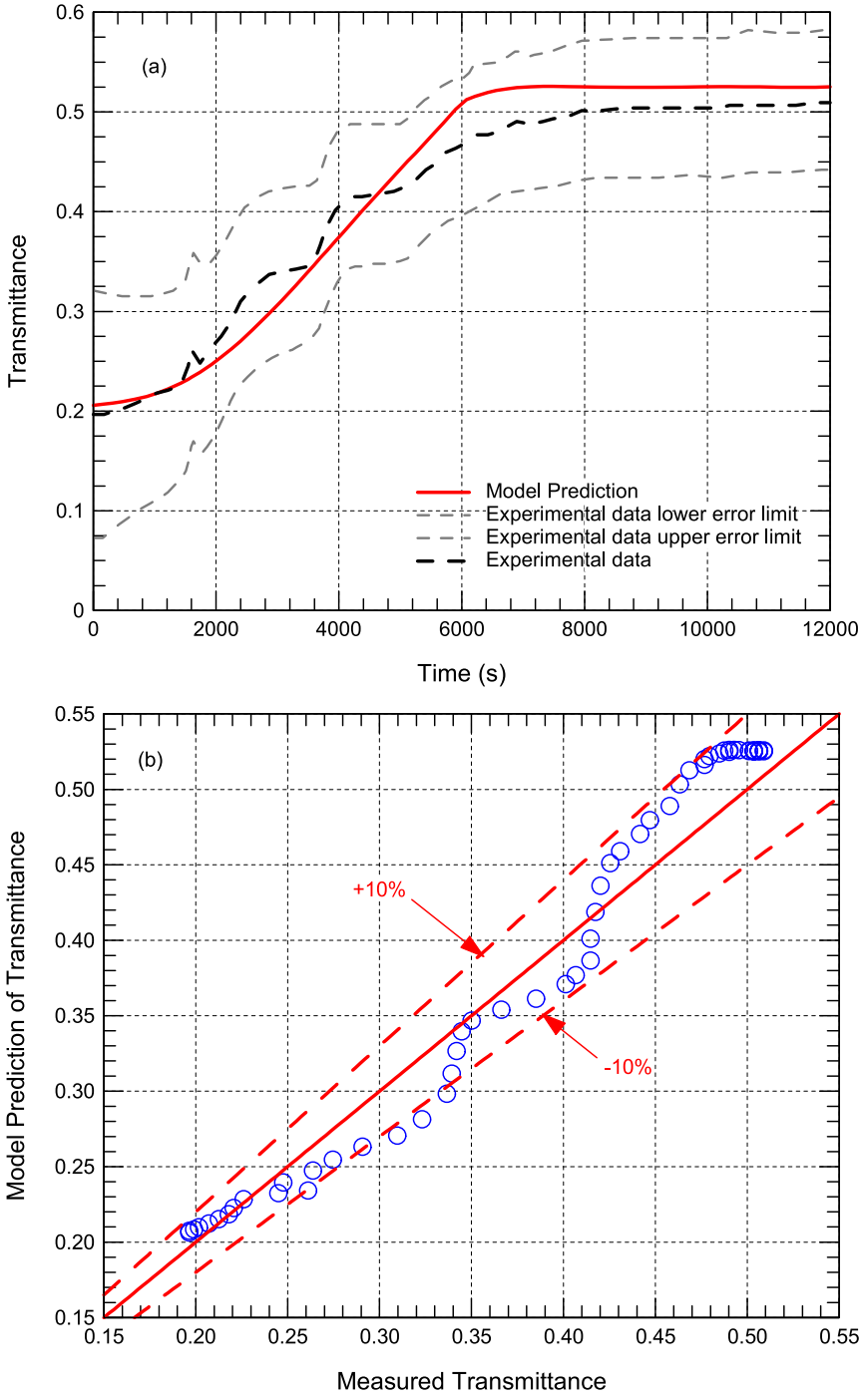

Fig. 2. Current numerical model results compared to the experimental data [28].

the mushy region as a porous medium, with porosity directly dependent on local temperature. Although this linearization simplifies the melting and solidification modeling, it introduces limitations, particularly where the experimental data indicate non-linear transitions. As shown in Fig. 2b, the numerical results fall within a ± 10 % range of the experimental values, thereby validating the model. This level of agreement confirms the model's suitability for simulating glazing systems incorporating SSPCMs in the present study.

$$d' = (\sigma_{a+}\sigma_s)s \tag{17}$$

$$\tau_{PCM} = 10^{-d'} \tag{18}$$

$$\sigma_a = \sigma_s\left[\frac{\tau_{PCM,liquid} - \tau_{PCM,solid}}{1 - \tau_{PCM,solid}}\beta + \frac{1 - \tau_{PCM,liquid}}{1 - \tau_{PCM,solid}}\right] \tag{19}$$

3.3. Grid and time-step sensitivity analysis

A grid and time-step sensitivity analysis are conducted to determine the optimal combination that ensures numerical accuracy while minimizing computational time. To evaluate the model sensitivity to spatial and temporal resolution, a series of simulations is performed using various mesh densities and time-step sizes. The time-averaged values of the air gap volume-averaged velocity (mm/s), air gap volume-averaged temperature (K), and glazing system heat energy (kJ) are presented in

Tables 2 and 3, facilitating direct comparison across different mesh and time-step sizes. The error is calculated using Eq. (20) for each mesh size and time-step. The goal is to confirm that the selected mesh and time-step adequately capture the key thermal and flow features of the system without introducing unnecessary computational load. Based on this analysis, a mesh containing 262,800 elements combined with a time-step of 300 s provide the most suitable compromise between accuracy and efficiency (i.e., the numerical solutions are approximately the same as those for finer mesh and smaller time-step). This configuration is therefore used for all simulations in the present study.

$$ith\ error = E_i = \frac{(F_{i+1} - F_i)}{F_i} \times 100 \tag{20}$$

where, F_i denotes the criterion parameter corresponding to each grid size and time step.

4. Results and discussion

This study investigates the energy and optical performance of the DGW-SSPCM system during the hottest and coldest days of 2022 in Montreal, Canada, under both sunny and cloudy conditions. A parametric analysis is conducted to assess the influence of glazing orientation and the transient thermal response of the SSPCM on system behavior across the four principal orientations: north, east, south, and west. Natural convection (NC) from buoyancy-driven flow within the air gap is included in all simulations to ensure accurate assessment of glazing system performance. Additional simulations excluding NC are performed to evaluate its impact and to determine whether it can be reasonably neglected to reduce computational cost without significantly compromising accuracy. The following sections present the results in a structured manner: the optical performance is first examined through the transient evolution of the transparency fraction over time; this is followed by a detailed analysis of fluid flow and heat transfer within the air gap, including the temperature difference across the air gap surfaces, velocity vector distributions, and the evaluation of Reynolds number (*Re*) and Raileigh number (*Ra*). The definitions of *Re* and *Ra* are provided in the Nomenclature, where the characteristic length for *Re* is the air gap depth (16 mm for DGW-R and 14 mm for DGW-SSPCM), and for *Ra* it is the air gap height (200 mm). The discussion then moves to the thermal behavior of the system and concludes with an evaluation of the overall energy performance.

4.1. Optical performance

Fig. 3 illustrates the variation of the transparency fraction of the SSPCM in the glazing system over a 24-h period for all orientations, with and without the consideration of NC, under both sunny and cloudy conditions during summer. The results indicate that the difference between the cases with and without NC is negligible. Throughout the summer period, the SSPCM completes its phase transition cycle across all orientations, regardless of whether the conditions are sunny or cloudy. During nighttime hours, the absence of solar radiation leads to a drop in the system temperature below the phase change freezing temperature threshold, resulting in the SSPCM remaining fully opaque. With sunrise, ambient temperature begins to rise, and the combined effect of direct and diffuse solar radiation contributes to the heating of the system. This thermal input triggers the phase transition by surpassing the melting temperature threshold of the soft segment within the molecular structure of the SSPCM, while the hard segment remains solid due to its higher melting point. As a result of this molecular structure, the material does not become liquid but instead gradually transitions to a transparent state. The latent heat storage capability of SSPCM moderates this process, as a defined quantity of energy must be absorbed to complete the phase transition from opaque to transparent.

In terms of orientation-specific behavior, the east-facing glazing system is the first to undergo phase change. It becomes fully transparent at approximately 6:00, begins transitioning back to the opaque phase around 18:00, and reaches full opacity by 22:00. The north-facing system follows, becoming fully transparent around 7:00, initiating its return to the opaque phase at approximately 21:00, and completing the transition by 23:00. The south-facing system reaches full transparency later in the day, around 10:00, while the west-facing system and the configuration under cloudy conditions achieve full transparency at approximately 14:00. These results suggest that the use of SSPCM in fenestration systems is particularly suited for commercial buildings. By tailoring the transition temperature, it is possible to achieve full transparency during typical office hours while simultaneously contributing to thermal regulation. This dual functionality supports visual comfort and energy efficiency during working periods. However, for residential applications, the application of SSPCM in residential glazing may offer limited visual benefits.

Fig. 4 presents the transparency fraction variation of the SSPCM in the glazing system over a 24-h period for all orientations, considering both the presence and absence of NC, under sunny and cloudy winter conditions. Unlike the summer results, the winter cases show a noticeable difference between simulations with and without NC. During the winter season, the SSPCM remains in its opaque state throughout the entire day for both the cloudy and north-facing scenarios, indicating that the available solar energy is insufficient to trigger a phase change. This highlights the limited solar gain on these surfaces under such conditions, preventing the SSPCM from absorbing the heat energy required to initiate the transition to a transparent state. In contrast, the east, south, and west orientations experience a complete phase transition cycle. Among them, the south-facing window exhibits the most favorable performance, achieving full transparency from 9:00 to 16:00. This

Table 2
Mesh sensitivity analysis.

No (i)	Number of Elements	v (mm/s)	Error (%)	$\overline{T}$ (K)	Error (%)	E (kJ)	Error (%)
1	33,300	15.12	88.76	300.624	0.0019	299.99	0.22
2	55,125	28.54	65.59	300.625	0.0017	299.34	0.11
3	95,256	9.82	106.92	300.627	0.0011	299.01	0.00
4	158,661	20.32	64.07	300.624	0.0019	299.02	0.07
5	262,800	7.30	4.11	300.626	0.0015	298.80	-0.01
6	360,672	7.00	3.43	300.626	0.0013	298.82	0.11
7	451,008	6.76	5.03	300.629	0.0003	298.49	-0.01
8	627,200	6.42	-	300.630	-	298.52	-

Table 3
Time-step study.

No (i)	Time-step size	v (mm/s)	Error (%)	$\overline{T}$ (K)	Error (%)	E (kJ)	Error (%)
1	1 hour	7.72	0.13	289.32	2.60	298.95	0.47
2	45 min	7.71	1.18	297.03	0.52	300.34	-0.46
3	30 min	7.62	0.93	298.57	0.34	298.95	-0.01
4	20 min	7.55	2.86	299.60	0.34	298.93	-0.03
5	10 min	7.34	0.55	300.63	0.17	298.84	-0.01
6	5 min	7.30	-1.75	301.14	0.09	298.80	0.00
7	2.5 min	7.43	-2.62	301.40	0.05	298.80	0.02
8	1 min	7.63	1.17	301.55	0.00	298.87	0.07
9	30 sec	7.72	-	301.55	-	299.08	-

extended duration of daylight transmission enhances the glazing system potential for natural lighting and passive solar heating during the cold season, making it particularly suitable for commercial buildings.

When comparing the system behavior with and without NC, the initiation of the phase change in the south-facing configuration occurs at approximately the same time in both cases. However, the presence of NC delays the time SSPCM reaches the opaque phase by about 30 min. Conversely, once the ambient temperature begins to drop and the SSPCM starts transitioning back from transparent to opaque, the presence of NC accelerates the onset of this reverse phase change by approximately 30 min compared to the case without NC. These results demonstrate that while NC has a limited impact on the overall duration of the transparent state, it can influence the dynamics of the transition process. The presence of NC contributes to more gradual thermal responses. This behavior further emphasizes the importance of accounting for NC effects when evaluating the performance of SSPCM-integrated glazing systems in cold climates.

4.2. Fluid flow and heat transfer analysis within air gap

This section analyzes the thermofluid behavior within the air gap of the glazing system under conditions where NC is present. Various parameters are examined to characterize the physical phenomena occurring inside the air gap and to establish a scientific basis for interpreting the system's energy performance under different seasonal and orientation-specific conditions.

4.2.1. Temperature difference across air gap

Fig. 5 presents the hourly variation of the area-weighted temperature difference across the air gap between the two facing surfaces within the glazing system. The results are shown for both the DGW-R and DGW-SSPCM systems under various seasonal conditions and orientations. As shown in Fig. 5, the temperature difference is considerably higher in winter than in summer. During winter, values typically range from 15 °C to 30 °C, mostly remaining above 25 °C, while in summer, the temperature difference stays between 0 and 5 °C throughout the 24-h period. This seasonal contrast reflects the stronger thermal gradient that exists during winter, when the indoor temperature is maintained at a much higher level than the cold exterior conditions, thereby intensifying buoyancy-driven flow. This would result in in obtaining lower thermal performance.

The effect of orientation is clearly observed, particularly in winter. The south-oriented configuration shows the lowest temperature difference among all orientations. This can be attributed to higher solar irradiation on the south-facing exterior surface, which increases the temperature of that surface and brings it closer to the indoor design temperature, thus reducing the overall thermal gradient across the air gap. In contrast, the north orientation as well as cloudy condition, which receive less solar radiation, exhibit higher temperature differences.

Differences between the DGW-R and DGW-SSPCM systems are also apparent. The phase change behavior of the SSPCM introduces a delay in thermal response, which becomes especially visible during the evening hours after approximately 16:00. As the ambient temperature drops, the SSPCM undergoes phase transition and releases the stored latent heat to the surrounding air gap. This process elevates the temperature of the SSPCM-facing surface, thereby causing both decrease and increase in the temperature difference compared to the DGW-R system based on the orientation. This behavior is most evident in winter, where the influence of latent heat release is more pronounced due to larger diurnal temperature swings.

4.2.2. Airflow velocity behavior within the air gap

For south-oriented DGW-SSPCM system as example, Figs. 6 and 7 present the velocity vector distribution within the air gap over a 24-h simulation period for summer and winter design days, respectively. The vectors are colored according to the velocity magnitude, depicting the development and evolution of airflow induced due to buoyancy-driven. These visualizations are used to evaluate transient flow structures within the air gap, which result from the temperature difference between the two internal-facing surfaces of the air gap, as described in Section 4.2.1. The results were obtained in a vertical slice passing through the mid-depth of the system (i.e., x = W/2), allowing a clear representation of the airflow pattern across the cavity height.

Fig. 6 shows the velocity vector distribution within the air gap of the south-oriented DGW-SSPCM system during the summer design day. The results reveal that the flow field remains weak and largely inactive during the nighttime and early morning hours, specifically between 00:00 and 08:00. This is attributed to the minimal temperature difference between the opposing surfaces of the air gap during this period, which results in insignificant buoyancy forces to drive the air movement.

Between 09:00 and 13:00, a slight increase in convective activity is observed, with upward motion developing near the sunlit exterior surface as solar irradiance induces surface heating. However, even during the peak solar hours from 11:00 to 14:00, the flow remains a quite weak where the velocity magnitudes do not exceed 0.05 m/s. The resulted flow lacks well-organized convective loops, indicating that the driving temperature gradient across the air gap remains small to sustain vigorous natural convection.

After 15:00, as solar input decreases and the exterior surface temperature begins to decline, the flow velocity further diminishes. The air within the air gap becomes approximately stagnant, and vector density drops, reflecting a return to conduction-dominant heat transfer. These results are consistent with the low temperature differences reported earlier in Section 4.2.1 (e.g., see Fig. 5) and confirm that NC plays a minimal role in heat transport within the glazing air gap under summer

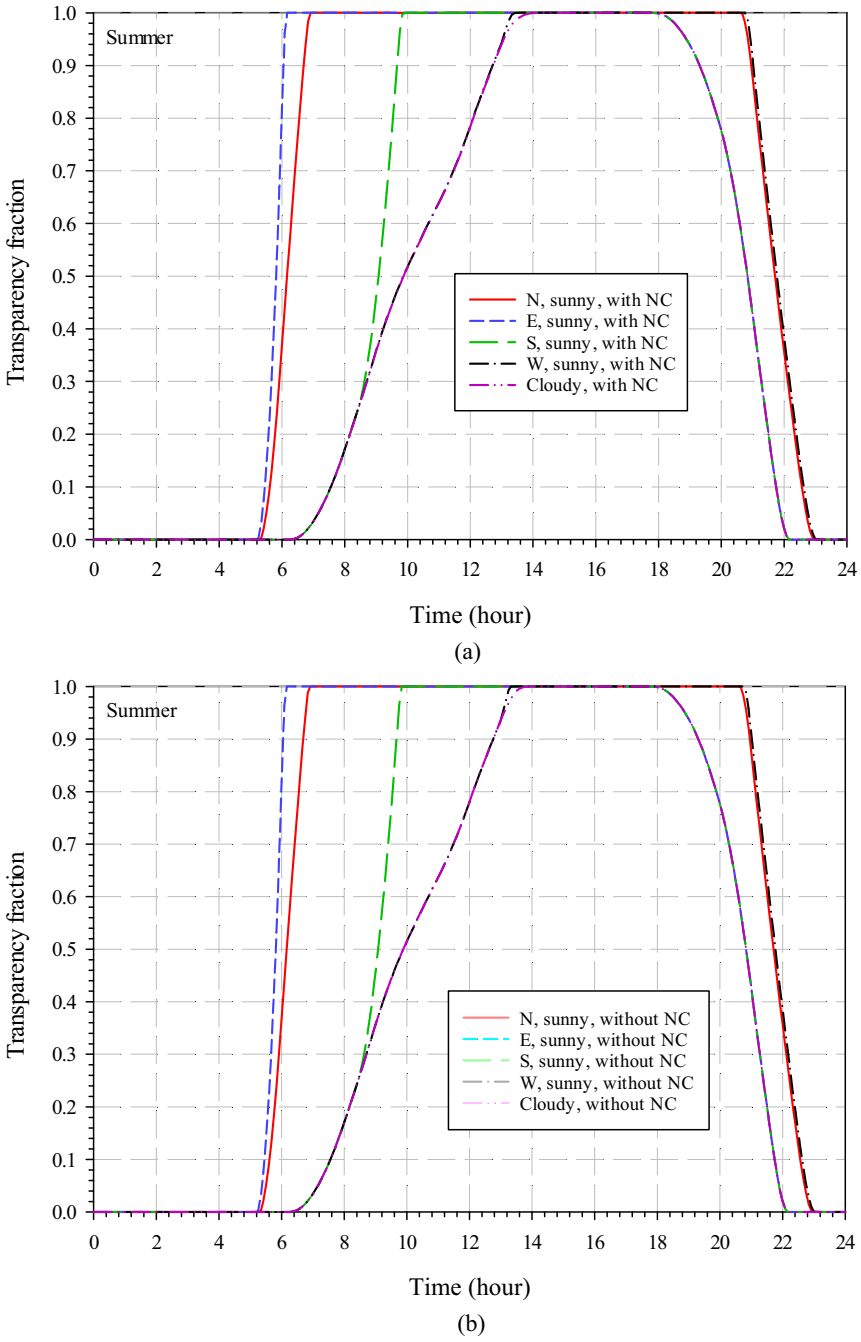

Fig. 3. Transparency fraction variation over a 24-h period for different orientations in DGW-R and DGW-SSPCM configurations, (a) with and (b) without NC, under summer conditions.

conditions.

Fig. 7 shows the velocity vector distribution within the air gap of the south-oriented DGW-SSPCM system during the winter design day. The results indicate that strong convective loops occur between 17:00 and 07:00, corresponding to the period with the highest temperature difference between the two opposing air gap surfaces (see Fig. 5). Note that the direction of the convection loop in winter is clockwise, whereas that in the summer is counter-clockwise. During this interval, the indoor surface remains consistently warm due to space heating, while the exterior surface temperature drops significantly, resulting in a strong thermal gradient across the air gap. This drives intensified buoyancy forces, leading to the formation of large, coherent convective loops at increased velocity magnitudes, with values reaching up to 0.14 m/s (about three times of that during the summer as shown in Fig. 6). Between 08:00 and 16:00, a noticeable weakening in the air flow pattern is observed. As solar radiation begins to heat the exterior surface, its temperature rises and approaches the indoor setpoint, thereby reducing the temperature difference across the air gap. This leads to a diminished buoyancy effect, as reflected by the lower velocity magnitudes during daylight hours.

These observations confirm that the strength of the air flow within the air gap is primarily governed by the instantaneous temperature gradient between the glazing surfaces. The cooling of the exterior surface during nighttime, combined with the latent heat release from the SSPCM, enhances the thermal driving potential and promotes stronger convective motion. In contrast, daytime solar gains reduce the temperature gradient and thereby suppress the flow intensity. This diurnal variation highlights the dynamic interplay between solar radiation,

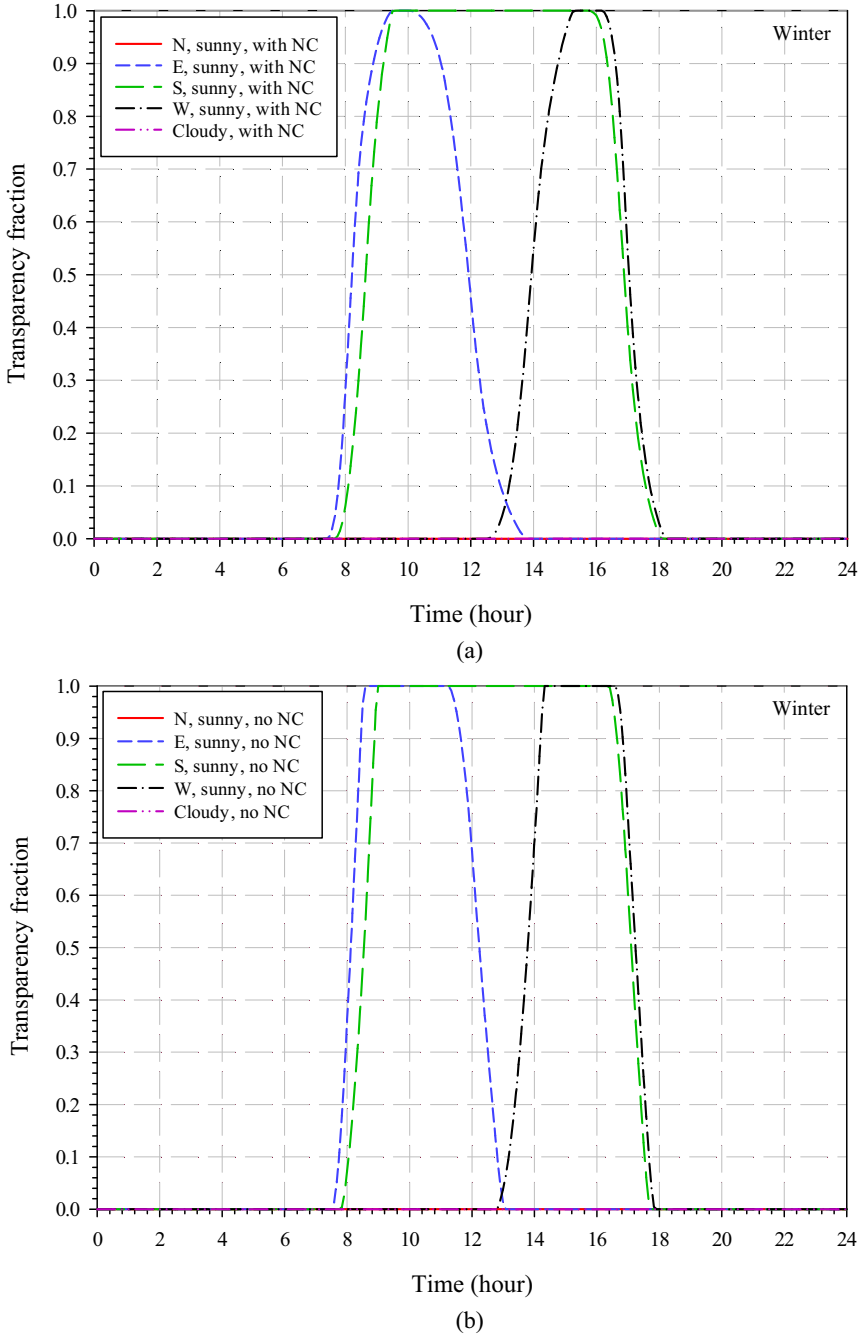

Fig. 4. Transparency fraction variation over a 24-h period for different orientations in DGW-R and DGW-SSPCM configurations, (a) with and (b) without NC, under winter conditions.

phase change effects, and air gap flow behavior in determining the transient thermal performance of the system.

4.2.3. Reynolds number

Fig. 8 illustrates the hourly variation of volume-averaged velocity within the air gap for both DGW-R and DGW-SSPCM systems across different orientations and seasonal conditions. This figure clearly highlights a significant difference in air flow velocity between summer and winter. In both systems, air velocities during summer predominantly range from 5 to 15 mm/s, whereas in winter they increase considerably, reaching values between 40 and 50 mm/s. This seasonal disparity is consistent with the temperature difference trends previously discussed (see Fig. 5), confirming that natural convection is more intense during colder conditions due to a stronger thermal gradient across the air gap. This figure also reveals that during summer, the air gap flow velocity reaches its minimum during nighttime and gradually increases to its peak during the daytime, following the rise in solar radiation. In contrast, the opposite pattern is observed in winter, where the flow velocity is lowest during the day and highest during the night, corresponding to the stronger temperature difference that develops after sunset.

A comparison between Fig. 8a and b reveals that the inclusion of the SSPCM results in a damping effect on the air gap velocity, particularly in winter. The latent heat storage of the PCM moderates temperature fluctuations within the air gap, reducing the temperature difference between the inner and outer surfaces. As a result, the buoyancy-driven airflow in the DGW-SSPCM system is slightly weaker than in the DGW-R configuration. This effect is most evident in winter, where the

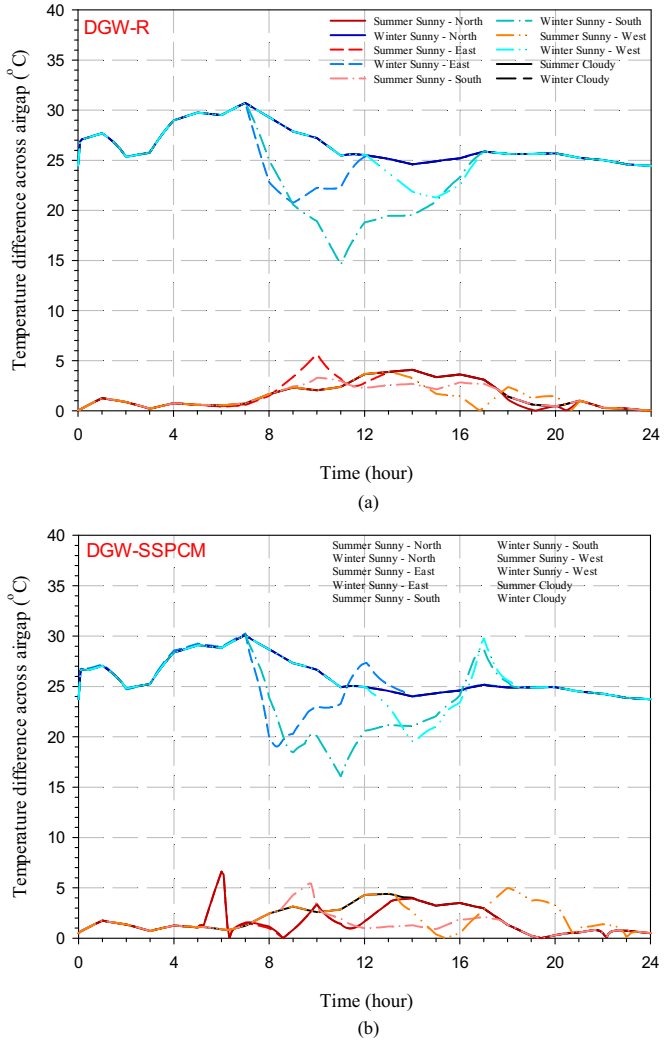

Fig. 5. Transient variation of temperature difference across the air gap in (a) DGW-R and (b) DGW-SSPCM systems over a 24-h period during summer and winter.

thermal buffering capacity of the SSPCM limits the peak velocities observed in the reference system. Although a general reduction in velocity is observed with the use of SSPCM, certain cases, such as the west orientation, show localized increases in velocity, particularly in the late afternoon and evening. This behavior is attributed to the heat released by the SSPCM after solar gains are reduced, which temporarily enhances the temperature gradient and sustains convective flow. This effect is visible in both summer and winter cases, highlighting the dynamic thermal response introduced by the phase change process.

Fig. 9 presents the Reynolds number values for the air within the glazing air gap for both DGW-R and DGW-SSPCM systems. The Reynolds number in summer ranges between 5 and 20, whereas in winter it increases significantly, reaching values between 40 and 53 depending on orientation. This clear seasonal contrast highlights the enhanced convective activity under colder conditions, driven by the stronger thermal gradient between the interior and exterior air gap surfaces. Across all cases, the Reynolds number remains within the laminar regime, indicating that while flow intensity varies significantly with season and orientation, the airflow does not reach transitional or turbulent conditions. These values serve as quantitative confirmation of the natural convection behavior observed in the velocity vector distributions and support the interpretation of flow regime characteristics in the subsequent analysis.

Fig. 10 presents the time-averaged values of the air gap flow velocity for all simulated cases across both seasons. The time-averaged velocity is substantially higher in winter for all cases, ranging from approximately 44.0 to 48.8 mm/s, compared to only 5.6 to 9.8 mm/s in summer. This seasonal disparity reaffirms the significant enhancement of NC during cold conditions due to the larger temperature difference between the indoor and outdoor surfaces. The DGW-R system consistently exhibits slightly higher velocities than DGW-SSPCM in winter, reflecting the moderating influence of the PCM, which reduces the temperature gradient and suppresses convective flow to some extent. In summer, however, the difference between the two systems is minimal.

Fig. 11 illustrates the corresponding time-averaged values of the air gap flow Reynolds number for all simulated cases across both seasons. In winter, time-averaged Reynolds numbers lie between approximately 44 and 49, confirming that the air gap flow remains in the laminar natural convection regime but with strong and sustained buoyancy-driven motion. In summer, the average Reynolds numbers remain well below 10.

The highest values for the time-averaged velocity and Reynolds number occur in the north and cloudy cases during winter for both DGW-R and DGW-SSPCM systems. In summer, however, the highest values are observed in the east-facing configuration for DGW-R and the west-facing configuration for DGW-SSPCM.

4.2.4. Rayleigh number

Fig. 12 presents the Rayleigh number values for the air within the glazing air gap for both DGW-R and DGW-SSPCM systems. The *Ra* is defined as $Ra = \frac{g\beta' \Delta T d^3}{\nu\alpha}$, where "d" denotes the air gap depth, which is used as the characteristic length in this study [40,41]. The most noticeable observation is the significantly higher fluctuation intensity of the Rayleigh number in summer compared to the relatively stable values in winter. These fluctuations are even more pronounced in the DGW-SSPCM system than in the DGW-R system, likely due to the dynamic phase change behavior of the PCM. Despite this, the overall Rayleigh number magnitudes remain nearly identical between the two systems with and without PCM in both seasons.

The Rayleigh number is a dimensionless parameter that governs the stability and transition from purely conductive to convective heat transfer, with higher values indicating the dominance of buoyancy-induced fluid motion over thermal diffusion. In this context, this figure shows that during summer, the Rayleigh number fluctuates mostly between 10^2 and 10^3. In contrast, during winter, the Rayleigh number consistently fluctuates around 10^4, clearly indicating the higher dominance of buoyancy-induced fluid motion over thermal diffusion in cold conditions. In this study, as the Rayleigh numbers for all systems with and without PCM were well below 10^5, the air flow in the glazing systems is laminar.

By factoring out all of the constant values in the Rayleigh number formulation, based on the assumptions applied for air properties in the present study, it can be expressed in the form $Ra = C.\Delta T/T^3$, where *C* is a constant and equal to 1.16×10^{10} K^2 for DGW-SSPCM and 7.79×10^9 K^2 for DGW-R. This expression highlights that the Rayleigh number is directly proportional to the temperature difference across the air gap (ΔT) and inversely proportional to the cube of the volume-averaged temperature within the air gap (T^3), highlighting its high sensitivity to thermal boundary conditions. Consequently, the higher temperature differences and lower average air gap temperatures in winter lead to substantially greater Rayleigh numbers and more intense buoyancy-driven convection compared to summer conditions. Furthermore, abrupt variations in temperature (T) during summer, driven by the onset of intense solar irradiation, lead to frequent fluctuations in the Rayleigh number.

Fig. 13 presents the time-averaged Rayleigh number for each simulated case, comparing seasonal and system-based variations. As expected, winter values are significantly higher across all orientations and both glazing systems, with values ranging from approximately 0.9×10^4

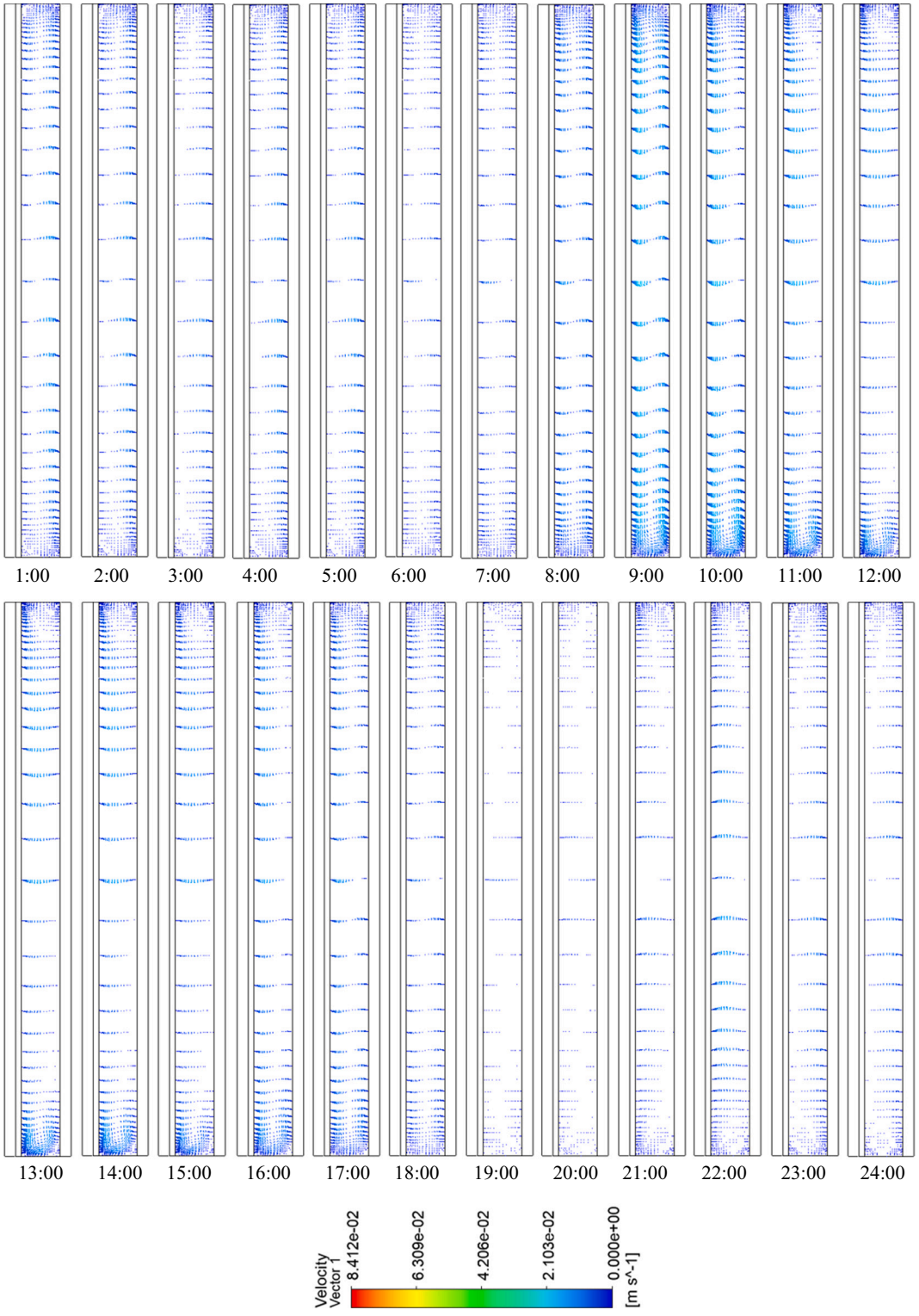

Fig. 6. Velocity vector distribution within the air gap of the south-oriented DGW-SSPCM system over a 24-h during summer period.

to 1.6×10^4. In contrast, summer values remain below 7.4×10^2, indicating higher conduction-dominated heat transfer within the air gap. The highest Rayleigh numbers are observed in the north and cloudy cases during winter for both DGW-R and DGW-SSPCM systems. These cases correspond to the largest temperature differences between the two air gap surfaces due to minimal solar gain on the exterior surface. Among all orientations, however, the south-facing cases consistently show the lowest values in winter, as solar heating raises the exterior surface temperature and reduces the thermal gradient. Additionally, the use of SSPCM leads to a slight reduction in the Rayleigh number across most winter cases. This is attributed to the PCM's ability to absorb and release heat, moderating the surface temperature difference and slightly lowering the buoyancy potential. In summer, the difference between the DGW-R and DGW-SSPCM systems is negligible.

It should be noted that the effect of the air gap difference between DGW-R and DGW-SSPCM is reflected implicitly in the results. The air

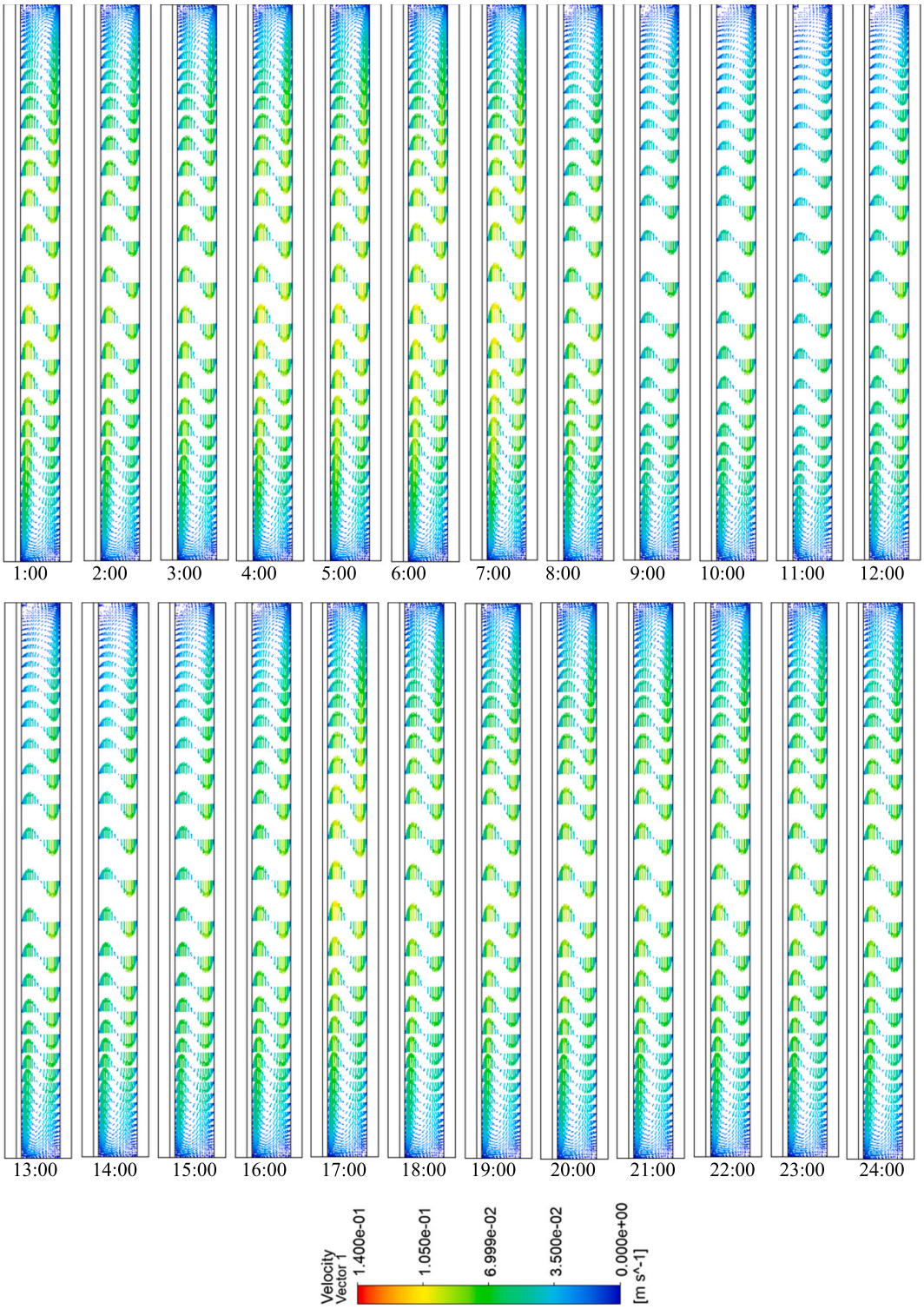

Fig. 7. Velocity vector distribution within the air gap of the south-oriented DGW-SSPCM system over a 24-h during winter period.

gap depth (d) is directly used as the characteristic length in the *Re* and *Ra* calculations (d = 16 mm for DGW-R and d = 14 mm for DGW-SSPCM), and it also influences the airflow velocity, which enters the *Re* calculation. Consequently, the impact of the 2 mm reduction in the air gap is implicitly captured in the velocity, *Re*, and *Ra* results.

4.3. Thermal analysis

This section presents the thermal performance evaluation of the DGW-SSPCM system across all studied configurations, with and without the inclusion of NC within the glazing air gap. In cases where NC is not considered, the air layer remains stagnant, and heat transfer occurs only through conduction and radiation. When NC is included in the model, convection is introduced as an additional heat transfer mechanism, which can enhance the overall thermal response of the system, resulting in lower energy performance. The objective of this comparative analysis is to assess the impact of NC on the system energy behavior, with particular attention to seasonal and orientation-dependent effects. It is

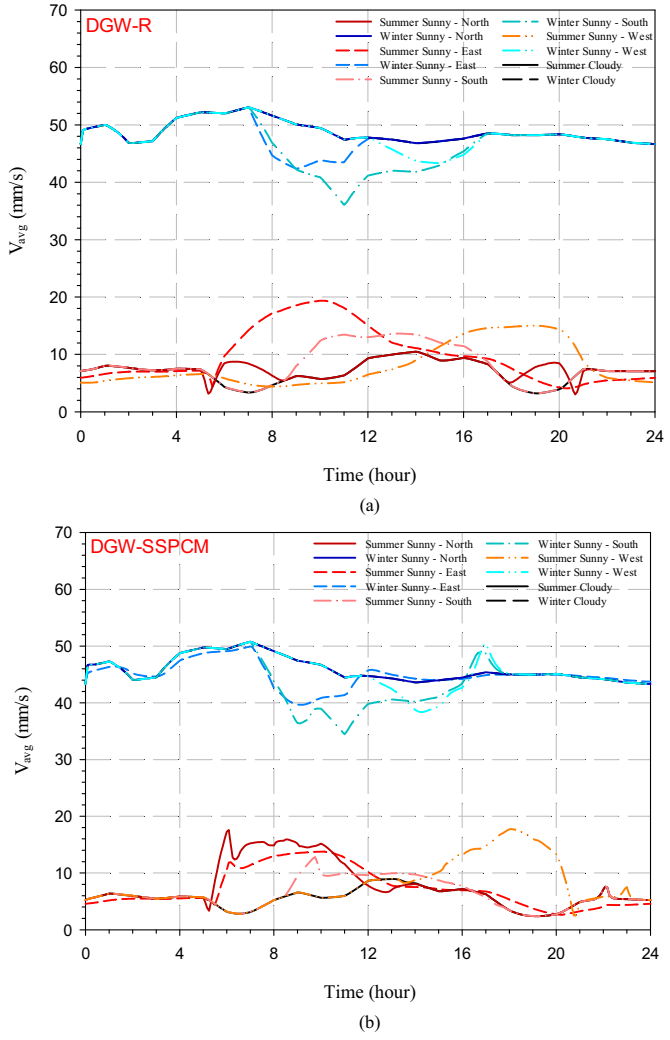

Fig. 8. Variation of volume-averaged air velocity within the glazing air gap over a 24-h period in (a) DGW-R and (b) DGW-SSPCM systems under summer and winter conditions.

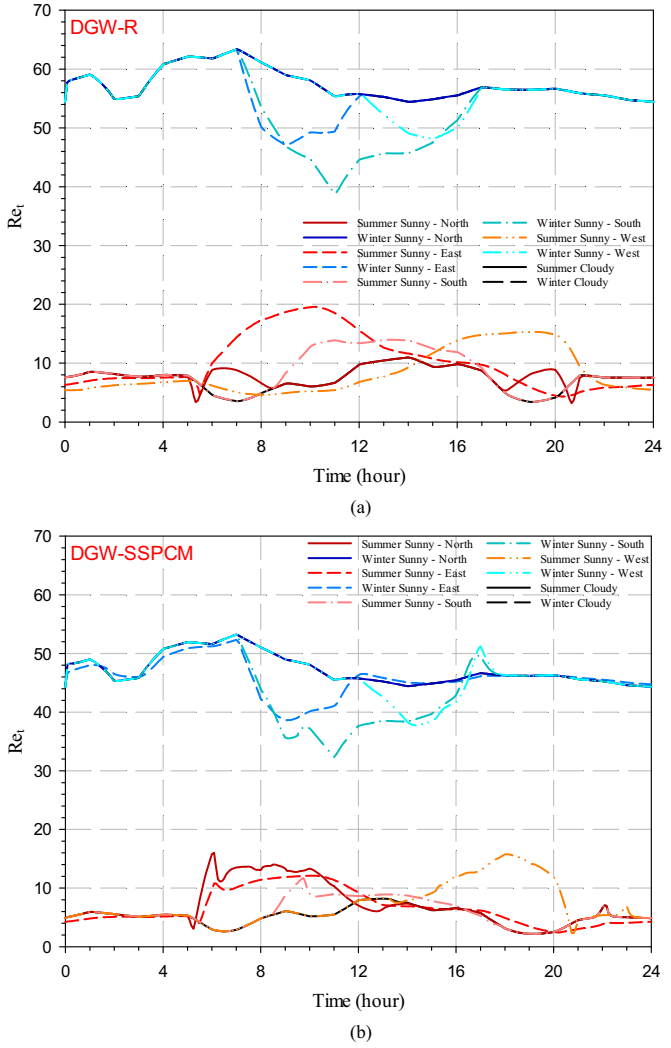

Fig. 9. Variation of Reynolds number within the glazing air gap over a 24-h period in (a) DGW-R and (b) DGW-SSPCM systems under summer and winter conditions.

important to recognize that incorporating NC significantly increases computational cost, typically by a factor of four to five compared to simulations that neglect it. Therefore, identifying scenarios where NC has a negligible influence can offer an opportunity to simplify the future simulations, reduce computation time, and maintain acceptable accuracy.

Fig. 14 illustrates the area-weighted average of interior surface temperature for the DGW-R system during summer for various orientations, with and without the inclusion of NC within the air gap. The results show that the impact of NC on the interior surface temperature remains negligible across all orientations and under both sunny and cloudy conditions. This observation is consistent with the previously noted minimal influence of NC on the transparency fraction, which is attributed to the weak buoyancy-driven airflow within the air gap during summer.

Under cloudy conditions, where direct solar radiation is absent, the interior surface temperature remains relatively stable, ranging between 22 °C and 26 °C throughout the day. In contrast, under sunny conditions, surface temperatures vary depending on orientation, with distinct peak periods corresponding to solar exposure. The east-facing configuration reaches its maximum surface temperature around 8:00, peaking at approximately 37.5 °C. The west-facing window exhibits a peak near 17:00, reaching about 36.5 °C. For the south-facing orientation, the highest surface temperature occurs around midday (13:00), reaching up to 32 °C. The north-facing configuration shows two moderate peaks, one in the early morning around 6:00 and another in the evening around 20:00, with surface temperatures rising to approximately 28 °C.

Fig. 15 presents the area-weighted average of interior surface temperature for the DGW-R system during winter for different glazing orientations, with and without the inclusion of NC within the air gap. The results indicate that NC has a noticeable impact on the interior surface temperature across all orientations and under both sunny and cloudy conditions. This behavior aligns with the previously observed significant influence of NC on the transparency fraction, which is driven by the strong buoyancy-induced airflow within the glazing air gap during winter.

Fig. 15 shows that for the north-facing configuration and under cloudy conditions, the interior surface temperature remains relatively low and stable throughout the day, ranging between 7 °C and 11 °C with no distinct peak. When NC is considered, the interior surface temperature is approximately 3.5 °C lower than the case without NC. This reduction further confirms the enhanced heat transfer within the system resulting from the addition of a new heat transfer mode, namely convection, which becomes active when NC is considered. In contrast, the other three orientations (east, south, and west) exhibit distinct peaks in surface temperature during the day under sunny conditions. Among these, the south-facing configuration reaches the highest peak, with the

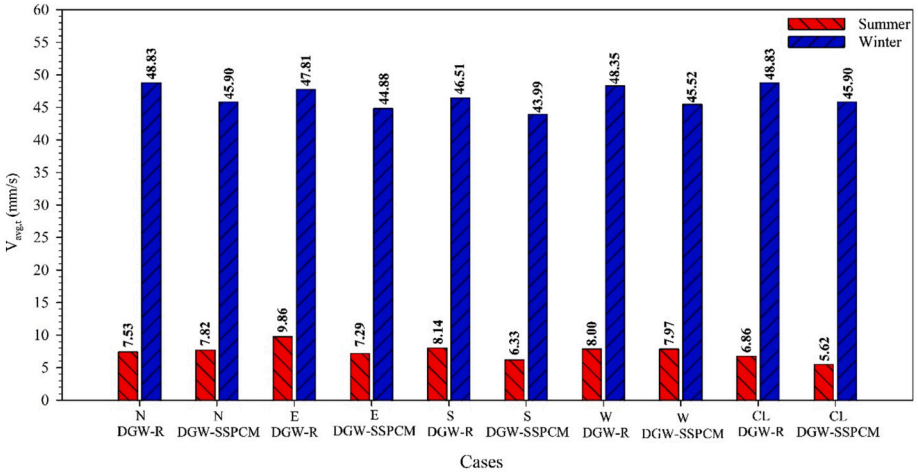

Fig. 10. Time-averaged of the volume-averaged air velocity within the glazing air gap for all orientations in DGW-R and DGW-SSPCM systems under summer and winter conditions.

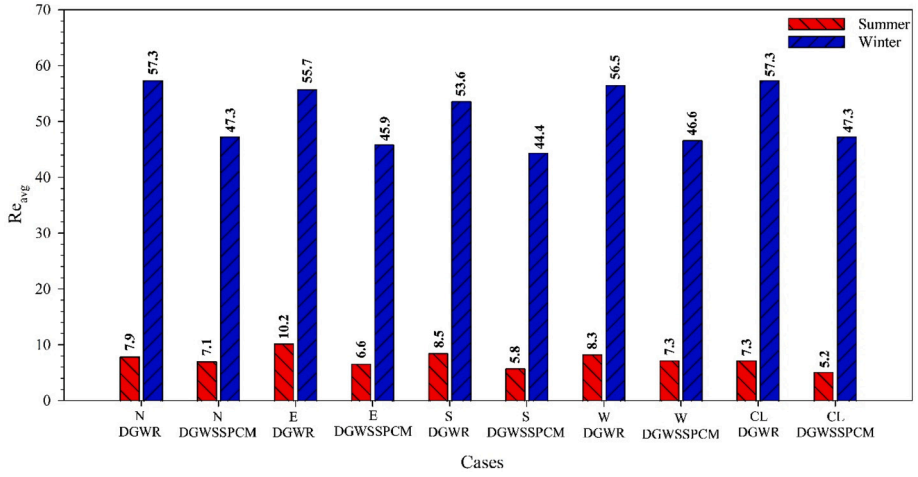

Fig. 11. Time-averaged Reynolds number within the glazing air gap for all orientations in DGW-R and DGW-SSPCM systems under summer and winter conditions.

inner surface temperature rising to approximately 27 °C around midday.

Fig. 16 illustrates the area-weighted average of interior surface temperature for the DGW-SSPCM system during summer for various glazing orientations, with and without the inclusion of NC within the air gap. Similar to the DGW-R configuration, the influence of NC on interior surface temperature remains negligible across all orientations and under both sunny and cloudy conditions. This observation is consistent with the limited buoyancy-driven flow within the air layer during summer, as discussed previously. A comparison between the results provided in Fig. 10 and Fig. 8 reveals that the incorporation of SSPCM introduces a delay in the rise of interior surface temperature following the onset of solar irradiation. This delay, attributed to the latent heat absorption of the SSPCM during phase transition, is particularly evident in the south-facing configuration, where solar exposure is more sustained. In addition, this delay contributes in enhancing the indoor air quality. Aside from this delay in temperature rise, the overall trend of interior surface temperature variation throughout the day in the DGW-SSPCM system closely follows that of the DGW-R system. However, during peak hours, the interior surface temperatures for the east-, south-, and west-facing orientations are slightly higher in the DGW-SSPCM system, reaching approximately 39.5 °C, 38.5 °C, and 33 °C, respectively. This increase can be associated with the thermal storage behavior of the SSPCM, which absorbs and releases heat over time, influencing short-term surface temperature dynamics. In contrast, under cloudy conditions and in the north-facing orientation, the peak surface temperatures are nearly identical between the DGW-SSPCM and DGW-R systems, due to the absence or limitation of direct solar radiation. Consequently, the proposed DGW-SSPCM system results in a slight reduction in indoor thermal comfort compared to the DGW-R system during summer. Furthermore, the inclusion of NC in the thermal modeling of both DGW-SSPCM and DGW-R systems is not essential for accurately predicting indoor thermal comfort under summer conditions, given the minimal impact observed on surface temperatures.

Fig. 17 presents the area-weighted average of interior surface temperature for the DGW-SSPCM system during winter for various glazing orientations, with and without the inclusion of natural convection (NC) within the air gap. Similar to the behavior observed in the DGW-R configuration under winter conditions, the impact of NC on interior surface temperature is notable in all cases. In the north-facing and cloudy scenarios, the inclusion of NC results in an approximate 2 °C decrease in interior surface temperature compared to the cases without NC. For the other orientations, the temperature difference between the NC and non-NC cases varies throughout the day, typically ranging between 1 and 3 °C. The most prominent influence of NC occurs during the phase when the SSPCM is releasing stored heat. When NC is considered, the temperature increase on the interior surface becomes more gradual, reflecting a smoother and more distributed heat release. This effect is attributed to the enhanced convective heat transfer within the air layer,

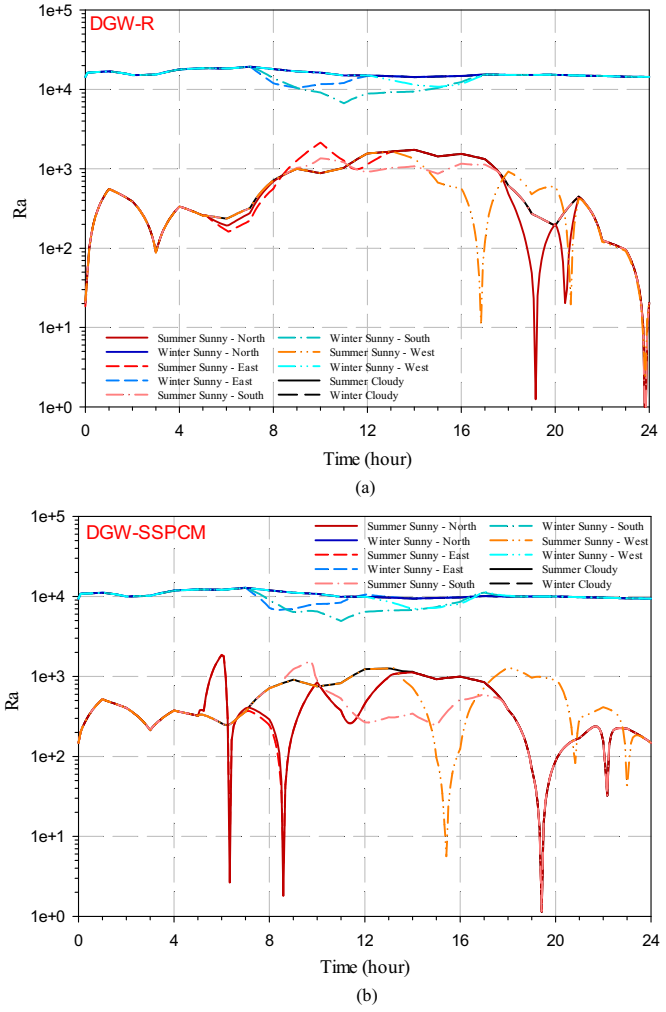

Fig. 12. Variation of the Rayleigh number within the glazing air gap over a 24-h period in (a) DGW-R and (b) DGW-SSPCM systems under summer and winter conditions.

which improves thermal distribution across the surface.

In addition, the interior surface temperatures of the DGW-SSPCM system are generally higher than those of the DGW-R system shown in Fig. 9. This confirms the thermal buffering capacity of the SSPCM and its effectiveness in enhancing indoor thermal comfort during winter conditions. Among the orientations, the east-, west-, and south-facing windows display distinct peaks in surface temperature, with the south-facing configuration reaching the highest value. The interior surface temperature in this case peaks around midday, reaching approximately 29 °C, as a result of direct solar exposure combined with latent heat release from the SSPCM. These results demonstrate the combined benefits of solar gain and latent thermal storage in achieving improved energy performance and occupant comfort in winter conditions.

Overall, the proposed DGW-SSPCM system improves indoor thermal comfort compared to the DGW-R configuration during winter. Additionally, incorporating NC in the thermal modeling of both systems is essential for accurately capturing indoor thermal conditions in the cold season, due to the significant influence observed on interior surface temperatures.

4.4. Energy analysis

Figs. 18 and 19 illustrate the total energy transfer for both DGW-R and DGW-SSPCM configurations across four orientations under sunny and cloudy conditions with and without the effect of natural convection (NC) in the air gap of the glazing systems. Fig. 18, corresponding to summer conditions, shows heat transfer from the outdoor environment into the indoor space, which represents the energy cooling load. In this context, when the energy value of the DGW-SSPCM values fall below those of DGW-R, this indicates improved energy efficiency related to the energy cooling savings. Fig. 19, representing winter conditions, displays the reverse heat transfer direction (from indoors to outdoors), which represents the energy heating load. In the cold season, lower energy values correspond to reduced heat loss, indicating improved energy efficiency related to the energy heating savings.

During summer, the data presented in Fig. 18 reveal that the total energy transferred across all orientations under cloudy conditions remains nearly the same between DGW-R and DGW-SSPCM systems. This behavior is largely attributed to the installation of the SSPCM layer on the interior surface of the glazing. During daytime hours, the SSPCM absorbs incident solar energy and stores it as latent heat, effectively not only dampening interior temperature fluctuations (see Fig. 16) but also reducing peak cooling demand. However, as ambient temperatures decline in the evening, the stored energy is released back into the indoor environment. While this delayed heat release can be beneficial in cooler climates, it contributes to internal heat gains that may be undesirable in warm conditions, particularly during the nighttime. As a result, the energy savings achieved by limiting heat gain during the day are counterbalanced by the additional heat released at night. This thermal compensation leads to approximately the same cumulative heat energy values over the full 24-h cycle for both DGW-SSPCM and DGW-R

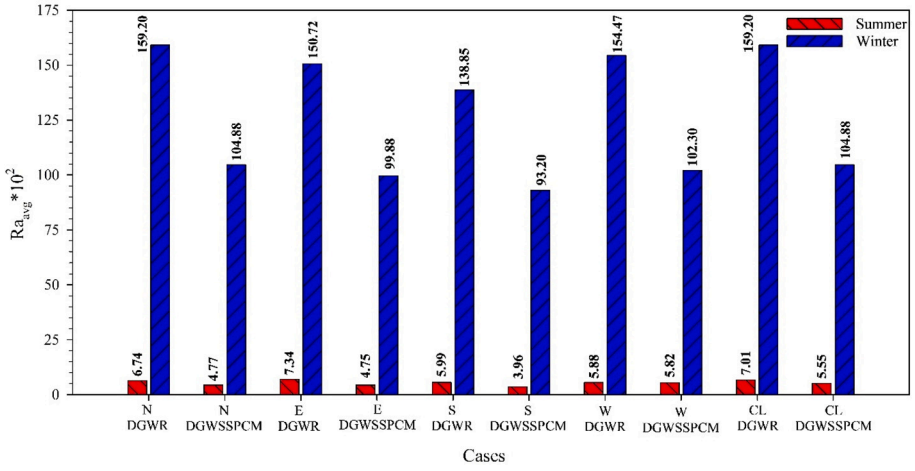

Fig. 13. Time-averaged Rayleigh number within the glazing air gap for all orientations in DGW-R and DGW-SSPCM systems under summer and winter conditions.

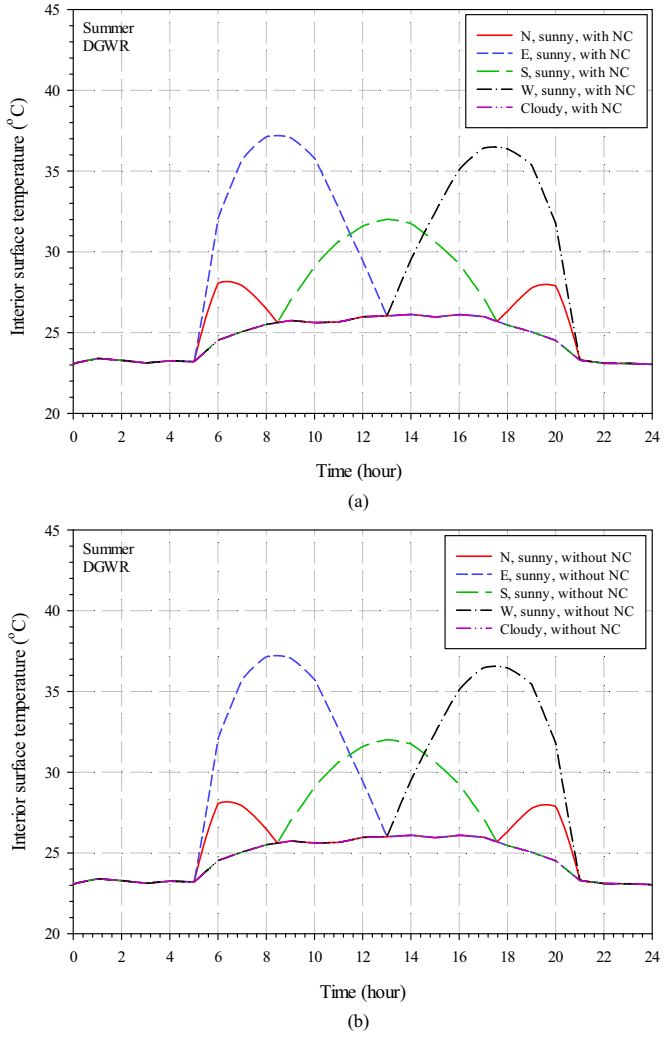

Fig. 14. Interior surface temperature variation over a 24-h period for different orientations in DGW-R configurations, (a) with and (b) without NC, under summer conditions.

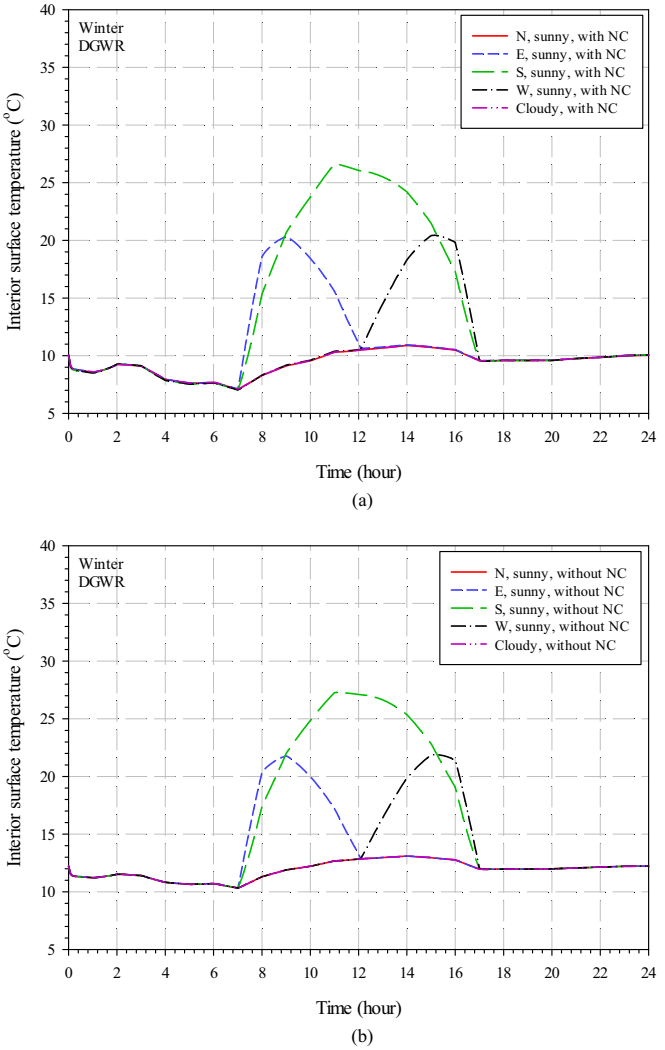

Fig. 15. Interior surface temperature variation over a 24-h period for different orientations in DGW-R configurations, (a) with and (b) without NC, under winter conditions.

configurations.

When comparing different orientations, the east-facing configuration exhibits the highest transmitted heat energy, reaching 297 kJ. This is followed by the west-facing window at 287 kJ, the south-facing window at 195 kJ, and the north-facing window at 112 kJ. The lowest transmitted heat energy is observed under cloudy conditions, with a value of 54 kJ. These results highlight the significant influence of solar exposure and orientation on the thermal performance of glazing systems during summer, emphasizing the need for orientation-specific design strategies to maximize the energy performance.

Fig. 18 demonstrates that the influence of NC is negligible across all orientations and under cloudy conditions. Therefore, when modeling DGW-R and DGW-SSPCM systems under summer climatic conditions in Montreal, the inclusion of NC is not essential. Neglecting NC in these scenarios is recommended, as its influence on the total energy transfer through the glazing system is minimal. Additionally, omitting NC consideration under summer conditions in Montreal can significantly reduce computational demands by a factor of four to five, without compromising the accuracy of energy performance predictions.

Fig. 19 illustrates the total energy transferred through the DGW-R and DGW-SSPCM systems, with and without considering NC, for various glazing orientations under both sunny and cloudy winter conditions. In contrast to the summer results, the winter data clearly show that the DGW-SSPCM configuration leads to consistent energy savings across all scenarios as a result of reducing heat loss through the fenestration system. This improvement is primarily attributed to the ability of the SSPCM to absorb solar energy and heat from the indoor air in the form of latent heat during the day and gradually release it back to the indoor space as outdoor temperatures decline. This behavior enables the system to passively regulating indoor temperatures and as well reducing the demand for active heating. Moreover, the effect of NC on the total transferred heat energy is pronounced during the winter season. The enhanced buoyancy-driven flow intensifies heat exchange within the air gap, further impacting the thermal performance of the glazing system. Therefore, accurately capturing NC effects is critical in winter conditions to avoid underestimating energy transfer.

The quantified energy savings for the DGW-SSPCM system relative to the DGW-R configuration are as follows: 21.7 kJ (3.5 %) for the north-facing window, 17.8 kJ (3.6 %) for the east-facing window, 19.1 kJ (3.8 %) for the west-facing window, 18.7 kJ (7.6 %) for the south-facing window, and 21.1 kJ (3.4 %) under cloudy conditions. These values demonstrate the DGW-SSPCM system capacity to improve energy efficiency in heating-dominated climates such as Montreal.

Fig. 19 also demonstrates that incorporating NC as an additional mode of heat transfer leads to increased energy loss compared to scenarios where NC is not considered. Specifically, for the DGW-R configuration, the total heat transfer is lower when NC is excluded, with the

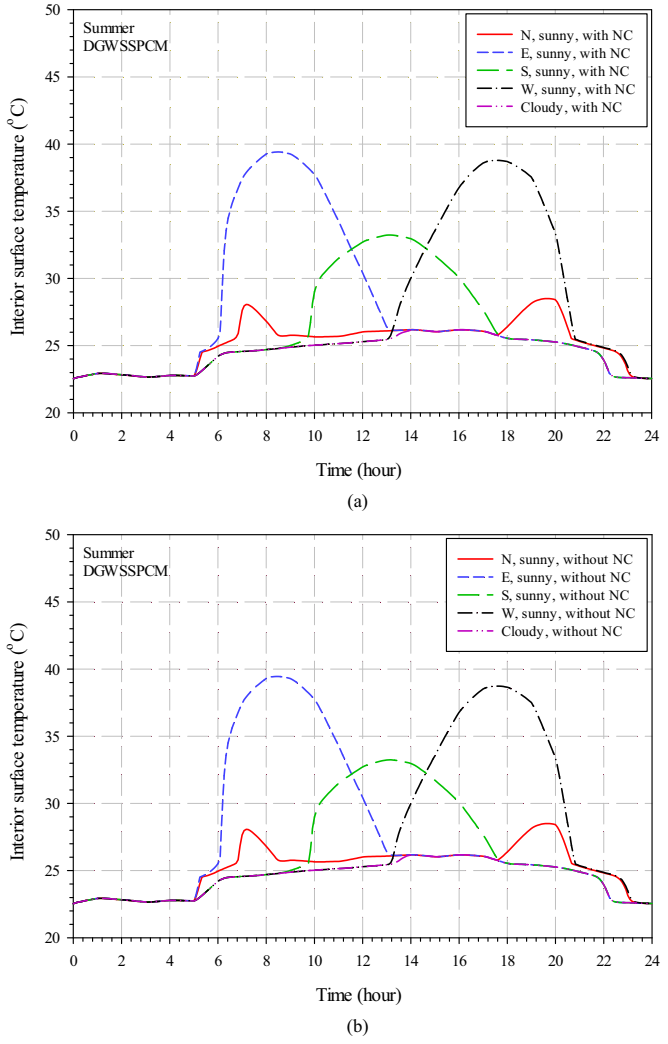

Fig. 16. Interior surface temperature variation over a 24-h period for different orientations in DGW-SSPCM configurations, (a) with and (b) without NC, under summer conditions.

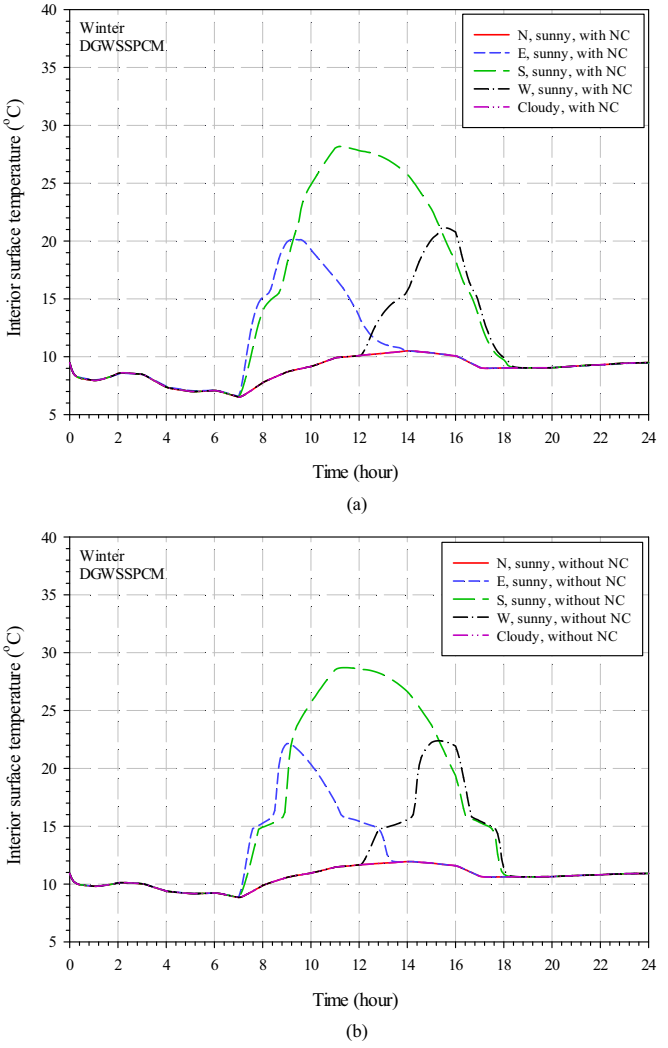

Fig. 17. Interior surface temperature variation over a 24-h period for different orientations in DGW-SSPCM configurations, with and without NC, under winter conditions.

differences quantified as follows: 86.9 kJ (14.2 %) for the north-facing window, 80.1 kJ (16.2 %) for the east-facing window, 73.6 kJ (29.9 %) for the west-facing window, 83.8 kJ (16.5 %) for the south-facing window, and 86.4 kJ (14.1 %) under cloudy conditions. Similarly, for the DGW-SSPCM configuration, the reduction in total heat transfer when NC is not considered is: 62.1 kJ (10.5 %) for the north-facing window, 57.9 kJ (12.1 %) for the east-facing window, 53.5 kJ (23.5 %) for the west-facing window, 60.6 kJ (12.4 %) for the south-facing window, and 62.2 kJ (10.5 %) under cloudy conditions. These results indicate that neglecting NC leads to an underestimation of total energy transfer by approximately 14 to 20 % in the DGW-R system and by 10 to 23 % in the DGW-SSPCM system.

Overall, for the weather condition of Montreal, the south-facing configuration is identified as the most effective option, as it provides the highest energy savings during the winter period while also maintaining full visual transparency during typical office hours. Based on the climatic conditions and simulation results, the optimal window design is a double-glazed unit incorporating a thin layer of SSPCM with a transition temperature of 15 °C, applied to the interior pane within the air gap and oriented toward the south. This configuration is recommended because the selected transition temperature ensures that the SSPCM remains fully transparent throughout the summer season, thereby preserving daylight availability and visual comfort. As demonstrated in the analysis, enabling a phase transition in summer does not result in a meaningful improvement in the thermal performance of the glazing system. In contrast, during winter, the SSPCM plays a significant role in reducing heat loss while maintaining visual transparency during the hours of occupancy. This dual benefit highlights the potential of the proposed system to enhance both energy efficiency and indoor environmental quality in cold climates.

5. Conclusion

This study investigated the energy and optical performance of a double-glazed window system incorporating a solid-solid phase change material (DGW-SSPCM) in comparison with a conventional reference system (DGW-R). Simulations were conducted under both sunny and cloudy conditions on the hottest and coldest days of year 2022 in Montreal, Canada, across the four main orientations (north, east, south, west). The aim was to evaluate the effectiveness of integrating a 2 mm SSPCM layer on the interior side of the glazing and assess the influence of Natural Convection (NC) within the window air gap, using detailed transient CFD modeling with the ANSYS FLUENT software. Both radiative and phase change phenomena were modeled using the Discrete Ordinates (DO) and solidification/melting models, respectively. The key findings are as follows:

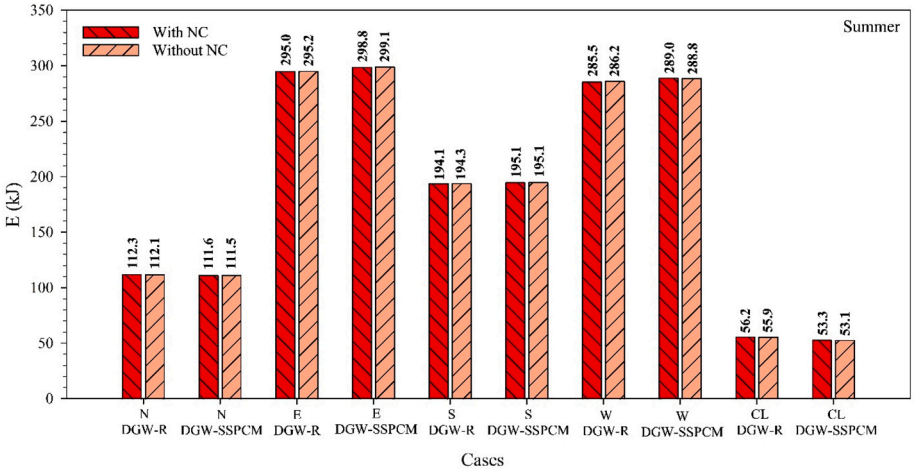

Fig. 18. Energy cooling load for DGW-R and DGW-SSPCM configurations in four orientations, North, East, West, and South, with and without NC, during summer.

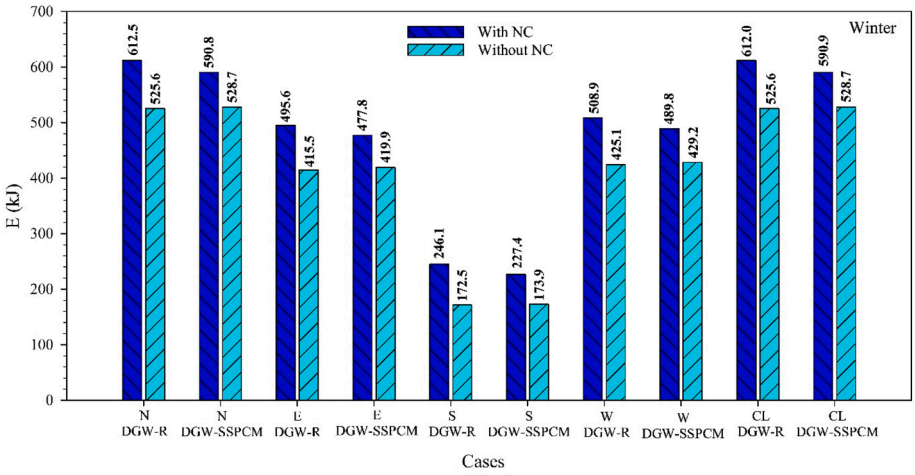

Fig. 19. Energy heating load for DGW-R and DGW-SSPCM configurations in four orientations, North, East, West, and South, with and without NC, during winter.

- Velocity analysis shows weak, conduction-dominant flow in summer (max 0.05 m/s) and organized convective loops in winter (up to 0.14 m/s).
- Airflow remains laminar in all cases, with Reynolds numbers of 5–20 in summer and 40–53 in winter. Highest values occur in north and cloudy cases during winter and in east (DGW-R) and west (DGW-SSPCM) orientations in summer.
- Rayleigh numbers reflect seasonal contrasts, with steady $\sim 1.3 \times 10^7$ in winter and fluctuating $\sim 10^6$ in summer, emphasizing sensitivity to temperature differences across the air gap.
- In summer, NC has negligible impact on energy and optical performance, so neglecting it can save computational time.
- In winter, NC raises interior surface temperatures (up to 3 °C), modifies SSPCM phase change, and affects transparency fraction, highlighting its importance for accurate predictions.
- DGW-SSPCM offers limited summer energy savings but reduces winter heat loss, achieving 3.4–7.6 % savings compared to DGW-R, with the south-facing orientation most efficient.
- Neglecting NC underestimates total energy transfer by 10–23 % depending on system and orientation, underscoring the need to model convective effects in cold conditions.
- SSPCM improves indoor thermal comfort in winter and slightly increases peak summer surface temperatures, making it more suitable for heating-dominated climates and commercial applications.

Under the climate conditions of Montreal, the recommended configuration is a south-facing DGW-SSPCM system, with the SSPCM placed on the interior glazing pane and designed with a transition temperature of 15 °C. This setup ensures that the material remains fully transparent and neutral in summer and activates its full latent heat potential during winter. The chosen configuration balances energy savings, thermal comfort, and daylight utilization, especially in commercial buildings with daytime occupancy.

Finally, integrating SSPCMs into glazing systems presents a promising passive solution to enhance energy efficiency and visual performance in cold climates. Future work should include annual-scale simulations with dynamic weather data to better quantify long-term benefits. Additionally, experimental validation under real-world conditions and development of SSPCMs with tunable or multi-stage transition behavior may further enhance adaptability and performance across broader climate contexts.

CRediT authorship contribution statement

Hossein Arasteh: Writing – original draft, Validation, Software, Methodology, Investigation, Formal analysis, Data curation, Conceptualization. **Wahid Maref:** Writing – review & editing, Supervision, Resources, Project administration. **Hamed H. Saber:** Writing – review & editing, Supervision, Project administration.

Declaration of competing interest

The authors declare that they have no known competing financial interests or personal relationships that could have appeared to influence the work reported in this paper.

Data availability

Data will be made available on request.

References

[1] B. Németh, A. Ujhidy, J. Tóth, J. Gyenis, T. Feczkó, Testing of microencapsulated phase-change heat storage in experimental model houses under winter weather conditions, Build. Environ. 204 (Oct. 2021) 108119, https://doi.org/10.1016/j.buildenv.2021.108119.

[2] National Research Council Canada (NRC), National Building Code of Canada, Ottawa, ON, Canada, 2020.

[3] S.B. Sadineni, S. Madala, R.F. Boehm, Passive building energy savings: A review of building envelope components, Renew. Sustain. Energy Rev. 15 (8) (Oct. 2011) 3617–3631, https://doi.org/10.1016/j.rser.2011.07.014.

[4] F. Roberz, R.C.G.M. Loonen, P. Hoes, J.L.M. Hensen, Ultra-lightweight concrete: energy and comfort performance evaluation in relation to buildings with low and high thermal mass, Energ. Buildings 138 (Mar. 2017) 432–442, https://doi.org/10.1016/j.enbuild.2016.12.049.

[5] Y. Ming, Y. Sun, X. Liu, X. Liu, Y. Wu, Thermal performance of an advanced smart fenestration systems for low-energy buildings, Appl. Therm. Eng. 244 (May 2024) 122610, https://doi.org/10.1016/j.applthermaleng.2024.122610.

[6] H. Arasteh, W. Maref, H.H. Saber, Energy and thermal performance analysis of PCM-incorporated glazing units combined with passive and active techniques: a review study, Energies 16 (3) (Jan. 2023) 3, https://doi.org/10.3390/en16031058.

[7] S.A. Moghaddam, C. Serra, M. Gameiro Da Silva, N. Simões, Comprehensive review and analysis of glazing systems towards nearly zero-energy buildings: energy performance, thermal comfort, cost-effectiveness, and environmental impact perspectives, Energies 16 (17) (Aug. 2023) 6283, https://doi.org/10.3390/en16176283.

[8] M.A. Ceviz, E. Mandev, B. Muratçobanoğlu, A. Çelik, F. Afshari, Experimental analysis of energy storage performance of phase change materials in horizontal double-glazing applications, J Energy Storage 73 (Dec. 2023) 108836, https://doi.org/10.1016/j.est.2023.108836.

[9] Y. Lu, et al., Optimization strategy for selecting the combination structure of multilayer phase change material (PCM) glazing windows under different climate zones, Sustainability 15 (23) (Nov. 2023) 16267, https://doi.org/10.3390/su152316267.

[10] M.A. Nsaif, J.M. Jalil, M. Baccar, An experimental and numerical investigation of the thermal performance of phase change materials in different triple-glazed window configurations, Int. J. Thermofluids 24 (Nov. 2024) 100889, https://doi.org/10.1016/j.ijft.2024.100889.

[11] D. Uribe, S. Vera, M. Perino, Development and validation of a numerical heat transfer model for PCM glazing: integration to EnergyPlus for office building energy performance applications, J Energy Storage 91 (June 2024) 112121, https://doi.org/10.1016/j.est.2024.112121.

[12] U.S. Department of Energy, EnergyPlus, Version 8.8.0: Building Energy Simulation Software, National Renewable Energy Laboratory, 2017 [Online]. Available: https://energyplus.net/.

[13] S. Shaik, et al., Glazing systems utilizing phase change materials: Solar-optical characteristics, potential for energy conservation, role in reducing carbon emissions, and impact on natural illumination, Energ. Buildings 311 (May 2024) 114151, https://doi.org/10.1016/j.enbuild.2024.114151.

[14] W. Hu, Y. Duan, D. Li, C. Zhang, H. Yang, R. Yang, Optimizing the indoor thermal environment and daylight performance of buildings with PCM glazing, Energ. Buildings 318 (Sept. 2024) 114481, https://doi.org/10.1016/j.enbuild.2024.114481.

[15] Z. Yuan, et al., Triple-glazed windows with phase change materials and aerogel: Thermal performance across diverse climate zones, Energy 330 (Sept. 2025) 136636, https://doi.org/10.1016/j.energy.2025.136636.

[16] Z. Zhang, M. Karkri, Y. Huang, Y. Wang, M.A. Tankari, L. Ibos, Experimental study on optical properties of paraffin-based phase change material glazing units and their performance optimization based on NSGA-II, J. Build. Eng. 108 (Aug. 2025) 112882, https://doi.org/10.1016/j.jobe.2025.112882.

[17] Z. Zhang, Y. Wang, Y. Huang, M. Karkri, M.A. Tankari, L. Ibos, Experimental study on optical properties of various paraffin-based PCM glazing unit and radiative transfer model optimization, Opt. Mater. 158 (Jan. 2025) 116431, https://doi.org/10.1016/j.optmat.2024.116431.

[18] E. Mandev, Enhancing thermoregulation in double glazed windows with PCMs and black films: an experimental study, Energ. Buildings 328 (Feb. 2025) 115171, https://doi.org/10.1016/j.enbuild.2024.115171.

[19] A. Fallahi, G. Guldentops, M. Tao, S. Granados-Focil, S. Van Dessel, Review on solid-solid phase change materials for thermal energy storage: molecular structure and thermal properties, Appl. Therm. Eng. 127 (Dec. 2017) 1427–1441, https://doi.org/10.1016/j.applthermaleng.2017.08.161.

[20] C.R. Raj, S. Suresh, R.R. Bhavsar, V.K. Singh, Recent developments in thermo-physical property enhancement and applications of solid solid phase change materials, J. Therm. Anal. Calorim. 139 (5) (Mar. 2020) 3023–3049, https://doi.org/10.1007/s10973-019-08703-w.

[21] G. Guldentops, G. Ardito, M. Tao, S. Granados-Focil, S. Van Dessel, A numerical study of adaptive building enclosure systems using solid–solid phase change materials with variable transparency, Energ. Buildings 167 (May 2018) 240–252, https://doi.org/10.1016/j.enbuild.2018.02.054.

[22] Y. Gao, et al., Parametric study of solid-solid translucent phase change materials in building windows, Appl. Energy 301 (Nov. 2021) 117467, https://doi.org/10.1016/j.apenergy.2021.117467.

[23] Y. Ma, et al., Energy and daylighting performance of a building containing an innovative glazing window with solid-solid phase change material and silica aerogel integration, Energy Convers. Manag. 271 (Nov. 2022) 116341, https://doi.org/10.1016/j.enconman.2022.116341.

[24] P. Wang, Z. Liu, L. Zhang, Z. Wang, J. Fan, Inversion of extinction coefficient and refractive index of variable transparency solid–solid phase change material based on a hybrid model under real climatic conditions, Appl. Energy 341 (July 2023) 121098, https://doi.org/10.1016/j.apenergy.2023.121098.

[26] C. Zhang, et al., Parametric research on thermal and optical properties of solid-solid phase change material packaged in glazing windows, J Energy Storage 83 (Apr. 2024) 110562, https://doi.org/10.1016/j.est.2024.110562.

[27] Effective Thermal Resistance of Plane Air Spaces; Chapter 26, Table 3, in: ASHRAE (Ed.), ASHRAE Handbook of Fundamental, ASHRAE: Peachtree Corners, Georgia, 2021, pp. 26.14–26.15.

[28] B.L. Gowreesunker, S.B. Stankovic, S.A. Tassou, P.A. Kyriacou, Experimental and numerical investigations of the optical and thermal aspects of a PCM-glazed unit, Energ. Buildings 61 (June 2013) 239–249, https://doi.org/10.1016/j.enbuild.2013.02.032.

[29] PCM Products, Accessed: May 19, 2024. [Online]. Available: https://www.pcmproducts.net/Phase_Change_Material_Products.htm.

[30] P. Wang, Z. Liu, L. Zhang, Z. Wang, J. Fan, Inversion of extinction coefficient and refractive index of variable transparency solid–solid phase change material based on a hybrid model under real climatic conditions, Appl. Energy 341 (July 2023) 121098, https://doi.org/10.1016/j.apenergy.2023.121098.

[31] Ansys Fluent, 2022. Canonsburg, PA, USA.

[32] A.D. Brent, V.R. Voller, K.J. Reid, Enthalpy-porosity technique for modeling convection-diffusion phase change: application to the melting of a pure metal, Numer. Heat Transfer 13 (3) (Apr. 1988) 297–318, https://doi.org/10.1080/10407788808913615.

[33] A.W.J. Heijs, C.P. Lowe, Numerical evaluation of the permeability and the Kozeny constant for two types of porous media, Phys. Rev. E 51 (5) (May 1995) 4346–4352, https://doi.org/10.1103/PhysRevE.51.4346.

[34] H.E. Beck, N.E. Zimmermann, T.R. McVicar, N. Vergopolan, A. Berg, E.F. Wood, Present and future Köppen-Geiger climate classification maps at 1-km resolution, Sci Data 5 (1) (Oct. 2018) 180214, https://doi.org/10.1038/sdata.2018.214.

[35] Historical Climate Data, Government of Canada, Accessed: Dec. 18, 2023. [Online]. Available: https://climate.weather.gc.ca/.

[36] H. Arasteh, W. Maref, H.H. Saber, Enhancing building energy efficiency: innovations in glazing systems utilizing solid-solid phase change materials, Therm. Sci. Eng. Prog. 55 (Oct. 2024) 102991, https://doi.org/10.1016/j.tsep.2024.102991.

[37] J. Chen, Q. Gong, L. Lu, Evaluation of passive envelope systems with radiative sky cooling and thermally insulated glazing materials for cooling, J. Clean. Prod. 398 (Apr. 2023) 136607, https://doi.org/10.1016/j.jclepro.2023.136607.

[38] F. Goia, M. Perino, M. Haase, A numerical model to evaluate the thermal behaviour of PCM glazing system configurations, Energ. Buildings 54 (Nov. 2012) 141–153, https://doi.org/10.1016/j.enbuild.2012.07.036.

[39] H. Arasteh, W. Maref, H.H. Saber, 3D numerical modeling to assess the energy performance of solid–solid phase change materials in glazing systems, Energies 17 (15) (Jan. 2024) 15, https://doi.org/10.3390/en17153759.

[40] R. Tafakkori, A. Fattahi, Introducing novel configurations for double-glazed windows with lower energy loss, Sustain Energy Technol Assess 43 (Feb. 2021) 100919, https://doi.org/10.1016/j.seta.2020.100919.

[41] R. Dalal, D. Naylor, D. Roeleveld, A CFD study of convection in a double glazed window with an enclosed pleated blind, Energ. Buildings 41 (11) (Nov. 2009) 1256–1262, https://doi.org/10.1016/j.enbuild.2009.07.024.